CFD modeling of biomass combustion and gasification in fluidized bed reactors using a distribution kernel method

Miao Yang[a], Jingyuan Zhang[b], Shenghui Zhong[a,c], Tian Li[b,d], Terese Løvås[b], Hesammedin Fatehi[a], Xue-Song Bai[a,*]

[a] *Department of Energy Sciences, Lund University, Lund 22100, Sweden*
[b] *Department of Energy and Process Engineering, Faculty of Engineering, NTNU - Norwegian University of Science and Technology, Trondheim, Norway*
[c] *State Key Laboratory of Engines, Tianjin University, 135 Yaguan Rd, Tianjin 300350, China*
[d] *RISE Fire Research, Tiller, Norway*

ABSTRACT

A three-dimensional reactive multi-phase particle-in-cell (MP-PIC) model is employed to investigate biomass combustion and gasification in fluidized bed furnaces. The MP-PIC model considered here is based on a coarse grain method (CGM) which clusters fuel and sand particles into parcels. CGM is computationally efficient, however, it can cause numerical instability if the clustered parcels are passing through small computational cells, resulting in over-loading of solid particles in the cells. To overcome this problem, in this study, a distribution kernel method (DKM) is proposed and implemented in an open-source CFD code, OpenFOAM. In DKM, a redistribution procedure is employed to spread the solid volume and source terms of the particles in the parcel to the domain in which the particles are clustered. The numerical stiffness problem caused by the CGM clustering can be remedied by this method. Validation of the model was performed using data from different lab-scale reactors. The model was shown to be able to capture the transient heat transfer process in a lab-scale bubbling fluidized bed reactor under varying fluidization velocities and loads of sand. Then, the model was used to study the combustion/gasification process in a bubbling fluidized bed reactor under varying ambient temperatures, equivalent air ratios, and steam-to-biomass ratios. The performance of DKM was shown to improve the accuracy and the robustness of the model.

© 2021 The Author(s). Published by Elsevier Inc. on behalf of The Combustion Institute.
This is an open access article under the CC BY license (http://creativecommons.org/licenses/by/4.0/)

1. Introduction

Biomass is considered a promising energy source because of its worldwide availability, ease of access, and renewable generation within a short period [1,2]. Biomass can be used in different applications, such as heat or power generation, chemical synthesis, and production of nanomaterials. Biomass can be transformed into liquid, gaseous, and solid fuels through different chemical, physical, and biological conversion processes [3]. As an alternative to fossil fuel for power generation and heating, biomass energy can contribute significantly towards the objectives of the UN's Paris Agreement in reducing greenhouse gas emissions. Fluidized beds (FB) have been adopted in coal/biomass gasification and combustion due to its high efficiency for gas-solid contact and advantage

of continuous operation [4]. Multi-scale and multi-physicochemical processes, such as complex hydrodynamics of dense gas-solid flow, particle collision, heat and mass transfer, radiation, homogeneous and heterogeneous chemical reactions, and turbulent combustion, occur simultaneously in a FB furnace [5]. Many experimental methods have been used to reveal the working mechanisms of FB [6,7]. The experimental methods have the disadvantage of high cost and long research cycles. Thus, the computational fluid dynamic (CFD) approach is considered as an efficient method for investigation of the complex gas-solid two-phase flow and combustion process [8].

Two main approaches are adopted to model gas-solid flow using CFD, the Euler–Euler approach and the Euler–Lagrange approach. In the Euler–Euler approach, both gas and solid phases are considered as the continuous phase while in the Euler–Lagrange approach, the gas phase is considered as a continuous phase and solid phase as a discrete phase [9]. In modeling fluid-solid interaction, the two-fluid model (TFM), developed based on the Euler–

Euler framework [10], has been extensively employed due to its low computational cost. The model is however unable to describe the properties of the solid-phase on the individual particle level, which makes it difficult to consider the distribution of the particle types and sizes since separate transport equations need to be solved for each size and type. Having many volume averaging and interpolation methods for both gas and solid phase can lead to accumulated numerical error and can result in a mesh-dependent solution.

In the framework of Euler–Lagrange approach, two groups of models are developed, discrete element method (DEM) [11] and multi-phase particle-in-cell (MP-PIC) method [12]. Compared with the Euler–Euler framework, the Euler–Lagrange approach can track each particle individually and the properties of the particles (diameter, density, velocity, temperature, and chemical composition, etc.) can be taken into account with a high accuracy [13]. This, however, leads to a sharp increase in the computational load, especially when the collision between the particles is considered. In the DEM model, the collision forces for each individual particle are calculated based on the interaction between all the individual particles in the system. The model has a high accuracy, but it is beyond the computational capacity to model industrial scale fluidized bed furnaces where quadrillion particles or more are involved. The MP-PIC model eliminates the difficulties of calculating interparticle interactions by mapping particle properties to an Euler grid and then mapping back computed stress tensors to particle positions [14]. This method was first developed by Andrews and O'Rourke [15]. MP-PIC is computationally much more efficient than the classical DEM method since more efficient collision models are used in the simulations and a much larger time step is allowed [9]. Recently, a general model for the numerical calculation of collisional exchange of mass, momentum, and energy between particles was presented [16], which uses a Bhatnagar, Gross, and Krook (BGK) model [17] in a transport equation for the particle distribution function, in order to approximate the rates at which the collisions bring about the local equilibrium of particle properties. In the BGK model, the effect of collisions is represented by a simple relaxation term on the right-hand side of the Boltzmann equation. A series of articles have been published reporting improved BKG-model collision damping time for particle velocity fluctuations [18] and the additional effect that drives the particle velocity distribution toward isotropy [19].

In an industrial-scale fluidized bed furnace, it is particularly important to reduce the computational load due to the presence of a large number of particles in the system. The coarse grain method (CGM), in which the virtual particles (known as parcels) are used to represent real particles, is widely employed in the Euler–Lagrange framework [20]. This method was discussed in detail in our previous work [21] that employed the CGM to simulate lab-scale fluidized beds. One of the characteristics of the CGM method is the high local carrier load in certain computational cells since the fuel and sand particles are clustered into parcels. This may cause problems in simulating industrial fluidized bed furnace with very complex geometries which leads to the presence of small computational cells, and a wide range of particle size distribution (PSD). Numerical instability and nonphysical over-load can occur when large virtual particles pass through small size cells. Large particles contribute to large source terms in the gas-phase governing equations which cause convergence problem or numerical artifacts due to large spatial gradients occurring in the small size cells [22]. This issue is particularly important in the most widely used and low-cost particle centroid method (PCM), in which the entire body of the particle is assumed to be in the local cell where the particle centroid is. At high particle load conditions, the solid volume fraction in the small local cell can be larger than that the cell can physically permit.

Different methods have been proposed to deal with the situation when the ratio of the mesh size to the particle size is too small, including the divided particle volume method (DPVM), the cube averaging method (CAM), the two-grid method (TGM), and the diffusion-based method (DBM) [22,23]. In our previous work [24], three of these methods, i.e., CAM, TGM, and DBM were investigated and their impact on the source term distribution was evaluated in a single-particle combustion case. In the DBM, the source terms of a Lagrangian particle are distributed into an Eulerian field according to a statistical kernel function. The source terms are calculated using the PCM model before the distribution, since the gas properties required by the particle sub-models are sampled from the particles' local cell. The DBM is more robust compared with the other investigated methods; however, the computational efficiency decreases rapidly with the increase of the mesh resolution. In the TGM, a virtual coarse grid is created based on the fine grid to solve the particle properties and the source terms are mapped to the fine grid [25]. The TGM, which treats the particles in a local grid, may cause significant errors for the simulations of particle-laden flows. In the CAM, a virtual cubic region is created as an interaction media between the particle and the gas phase. Compared with the TGM and the DBM, the CAM has an obvious advantage in computational efficiency for dense multiphase flow with unstructured meshes. However, two independent meshes need to be constructed in the CAM, which increases the complexity of the implementation and parallel computation.

The purpose of this work is to develop a comprehensive MP-PIC model taking into account chemical reactions to investigate the performance of dense gas-solid fluidized bed reactors. The focus is on developing a robust method that can handle the local over-load problem in small-size grid cells. In Section 2 we present the basic mathematical framework of the Euler–Lagrange governing equations and the mathematical formulation for the DKM. In Section 3 we introduce the numerical methodology to solve the Euler–Lagrange governing equations, as well as the cell searching strategy and parallel computation method for the DKM. The validation of the model and the performance of the DKM are discussed in Section 4 and the conclusions are presented in Section 5.

2. Mathematical formulation

In the MP-PIC approach, the governing equations of the continuous phase and the discrete phase are described in the Euler and Lagrange frameworks, respectively. The interaction between the discrete and the continuous phase is modeled using the mass, momentum and energy source terms. The mass conservation and energy conservation equations are adopted from Refs. [26–28] and the momentum equations are adopted from Refs. [28,29]. The physical interpretation of the terms in the governing equations is not discussed in detail, but the reader is referred to the previous publications for further details.

2.1. Gas phase governing equations

In numerical simulations of fluidized bed furnaces, Reynolds averaged Navier–Stokes (RANS) turbulence closure is often used. The gas phase governing equations consist of the Reynolds-averaged continuity, momentum, energy and species transport equations. The continuity equation is

$$\frac{\partial \left(\alpha_g \overline{\rho_g} \right)}{\partial t} + \nabla \cdot \left(\alpha_g \overline{\rho_g} \widetilde{\mathbf{u}}_g \right) = \overline{S}_m, \tag{1}$$

where the overbar denotes that the quantity is Reynolds averaged, and the tilde denotes Favre averaged. α_g is the gas volume fraction, ρ_g is the gas density, $\mathbf{u}_g$ is the velocity vector of the gas, and S_m

represents the gas formation rate due to thermochemical conversion of the fuel particles. The momentum equations are

$$\frac{\partial\left(\alpha_g\overline{\rho}_g\widetilde{\mathbf{u}}_g\right)}{\partial t} + \nabla\cdot\left(\alpha_g\overline{\rho}_g\widetilde{\mathbf{u}}_g\widetilde{\mathbf{u}}_g\right) = \alpha_g\overline{\rho}_g\mathbf{g} - \alpha_g\nabla\overline{p}_g + \nabla\cdot\left(\alpha_g\overline{\tau}_g\right) + \overline{\mathbf{S}}_u, \tag{2}$$

where $\mathbf{g}$ is the gravitational acceleration, p_g is the gas pressure, τ_g is the sum of viscous stress and Reynolds stress, and $\mathbf{S}_u$ is the source term due to momentum exchange between the gas and the solid phase. The energy equation is

$$\frac{\partial\left(\alpha_g\overline{\rho}_g\left(\widetilde{h}+\widetilde{K}\right)\right)}{\partial t} + \nabla\cdot\left(\alpha_g\overline{\rho}_g\widetilde{\mathbf{u}}_g\left(\widetilde{h}+\widetilde{K}\right)\right) = \alpha_g\overline{\rho}_g\widetilde{\mathbf{u}}_g\cdot\mathbf{g} + \frac{\partial\alpha_g\overline{p}_g}{\partial t}$$
$$+\nabla\cdot\left(\alpha_g\overline{\rho}_g\Gamma_{eff}\nabla\widetilde{h}\right) + \alpha_g\overline{Q}_r + \alpha_g\overline{Q}_{com} + \overline{S}_q, \tag{3}$$

where h is the specific enthalpy of the gas, and K is the kinetic energy of the gas flow. Γ_{eff} is the sum of molecular and turbulent heat diffusion coefficients, $\Gamma_{eff} = \Gamma_g + \mu_t/(\overline{\rho}_g Pr_t)$, where Pr_t is the turbulent Prandtl number and μ_t is the turbulent eddy viscosity. $\overline{Q}_r$ is the mean source term due to radiative heat transfer, $\overline{Q}_{com}$ is the mean source term due to volatile chemical reactions, and $\overline{S}_q$ is the mean source term due to thermochemical conversion of the solid fuel. The species transport equation is

$$\frac{\partial\left(\alpha_g\overline{\rho}_g\widetilde{Y}_{g,k}\right)}{\partial t} + \nabla\cdot\left(\alpha_g\overline{\rho}_g\widetilde{\mathbf{u}}_g\widetilde{Y}_{g,k}\right) = \nabla\cdot\left(\alpha_g\overline{\rho}_g D_{eff}\nabla\widetilde{Y}_{g,k}\right) + \alpha_g\overline{\dot{\omega}}_{g,k}$$
$$+\overline{S}_{Y_k}, \tag{4}$$

where $Y_{g,k}$ is the mass fraction of species k in the gas mixture, and $\overline{\dot{\omega}}_{g,k}$ is the mean chemical reaction rate of species k. D_{eff} is the effective mass diffusion coefficient for species k taking both the viscous and turbulent contributions into account, $D_{eff} = D_g + \mu_t/(\overline{\rho}_g Sc_t)$, where Sc_t is the turbulent Schmidt number. $\overline{S}_{Y_k}$ is the mean formation rate of species k due to thermochemical conversion of the solid fuel particles.

A Partially Stirred Reactor (PaSR) model is used to account for turbulence chemistry interaction when computing the source terms due to gas phase chemical reactions ($\overline{\dot{\omega}}_{g,k}$, $\overline{Q}_{com}$) [30]. In the PaSR model, the mean reaction rates are modeled as

$$\overline{\dot{\omega}}_{g,k} = \kappa\dot{\omega}_{g,k}(\widetilde{Y}, \widetilde{T}, \overline{p}), \tag{5}$$

where κ is the volume fraction of the reactive mixture, $\kappa = \frac{\tau_c}{\tau_c + \tau_m}$. τ_c and τ_m denote the local chemical reaction time and the local mixing time, respectively. The chemical reaction time, τ_c, is determined from the mean reaction rates of the fuel ($\overline{\dot{\omega}}_f$) and the oxidizer or the gasification agents ($\overline{\dot{\omega}}_o$),

$$\frac{1}{\tau_c} = max\{\frac{-\overline{\dot{\omega}}_f}{Y_f}, \frac{-\overline{\dot{\omega}}_o}{Y_o}\}, \tag{6}$$

where subscripts f and o denote the fuel and oxidizer or the gasification agents, respectively. The mixing time τ_m is modeled as

$$\tau_m = C_{mix}\sqrt{\frac{\nu}{\varepsilon}}, \tag{7}$$

where C_{mix}, is a model constant ($C_{mix} = 1.0$ in this study). ν and ε denote the kinematic viscosity and the dissipation rate of turbulent kinetic energy, respectively.

The stress tensor $\overline{\tau}_g$ in the Eq. (2) is the sum of the viscous and Reynolds stresses and can be written as

$$\overline{\tau}_g = \overline{\tau}_l + \overline{\tau}_t. \tag{8}$$

The stress tensor for a Newtonian fluid is expressed as

$$\overline{\tau}_l = \mu_g((\nabla\widetilde{\mathbf{u}}_g) + (\nabla\widetilde{\mathbf{u}}_g)^T - \frac{2}{3}(\nabla\cdot\widetilde{\mathbf{u}}_g)\mathbf{I}), \tag{9}$$

and the Reynolds stresses are modeled according to

$$\overline{\tau}_t = \mu_t((\nabla\widetilde{\mathbf{u}}_g) + (\nabla\widetilde{\mathbf{u}}_g)^T - \frac{2}{3}(\nabla\cdot\widetilde{\mathbf{u}}_g)\mathbf{I}) - \frac{2}{3}\overline{\rho}_g k\mathbf{I}, \tag{10}$$

where μ_g is the dynamic viscosity, and $\mathbf{I}$ is the second order unit tensor. Standard $k-\varepsilon$ model is used to determine the eddy viscosity, $\mu_t = \overline{\rho}_g C_\mu k^2/\varepsilon$, where k is the turbulent kinetic energy. k and ε are modeled using the following transport equations:

$$\frac{\partial\left(\alpha_g\overline{\rho}_g k\right)}{\partial t} + \nabla\cdot\left(\alpha_g\overline{\rho}_g\widetilde{\mathbf{u}}_g k\right) = \nabla\cdot\left(\alpha_g\left(\mu_g + \frac{\mu_t}{\sigma_k}\right)\nabla k\right)$$
$$+\alpha_g P_k - \alpha_g\overline{\rho}_g\varepsilon + S_k, \tag{11}$$

$$\frac{\partial\left(\alpha_g\overline{\rho}_g\varepsilon\right)}{\partial t} + \nabla\cdot\left(\alpha_g\overline{\rho}_g\widetilde{\mathbf{u}}_g\varepsilon\right) = \nabla\cdot\left(\alpha_g\left(\mu_g + \frac{\mu_t}{\sigma_\varepsilon}\right)\nabla\varepsilon\right)$$
$$+\alpha_g\frac{\varepsilon}{k}\left(C_{\varepsilon_1}P_k - C_{\varepsilon_2}\overline{\rho}_g\varepsilon\right) + S_\varepsilon, \tag{12}$$

where $P_k = \overline{\tau}_t : \nabla\widetilde{\mathbf{u}}_g$ is the production rate of turbulent kinetic energy. S_k and S_ε are the source terms due to gas–solid interaction. Standard values of model constants are used, $C_\mu = 0.09$, $C_{\varepsilon 1} = 1.44$, $C_{\varepsilon 2} = 1.92$, $C_{\sigma k} = 1.0$ and $C_{\sigma\varepsilon} = 1.3$ [5,31].

2.2. Solid phase governing equations

Two types of particles, biomass and sand, exist in the solid phase. During the thermochemical conversion process of biomass particles, the sand particles are assumed to be chemically inert. The interaction between the particles and the surrounding gas is through mass and momentum exchange and heat transfer. The mass, momentum, and energy conservation equations for solid phase in the MP-PIC model are described in the following.

2.2.1. Mass conservation equation and pyrolysis models

Biomass particle conversion (direct combustion/pyrolysis and gasification) can be seen as a two-stage process: pyrolysis (or devolatilization) and heterogeneous conversion of char [32,33]. The pyrolysis product consists of heavy hydrocarbon species (such as tar), light hydrocarbon species (such as methane), water, carbon monoxide, and carbon dioxide, etc. Pyrolysis models including detailed tar species have been reported (e.g., [34]) and used in our previous studies of single particle combustion [35]. The aim of this work is to develop a robust MP-PIC model that can be used to study a wide range of particle loads. Hence, a one-step pyrolysis model and a simplified homogeneous volatile gas and heterogeneous char reaction mechanism are employed in the present work, following the literature [5,8,21,31,36–40]. However, more advanced and complex chemical kinetic models (e.g., including tar chemistry) [34,41,42] can be employed in the developed model framework. The one-step pyrolysis reaction model is

$$Biomass \rightarrow x_1 CO + x_2 CO_2 + x_3 H_2O + x_4 H_2 + x_5 CH_4$$
$$+x_6 Ash_{(s)} + x_7 C_{(s)}, \tag{13}$$
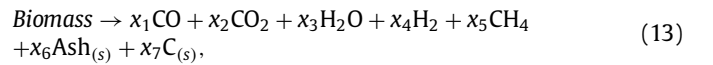
where x_j are the stoichiometric constants. $Ash_{(s)}$ and $C_{(s)}$ denote respectively ash and char that are in solid phase.

Heterogeneous reactions of char with the surrounding gas species (such as O_2, CO_2, H_2O) is a complex process, involving char-O_2, char-CO_2 and char-H_2O reactions. High molecular weight hydrocarbons (tar) are treated as unstable products and reactions with sulfur and nitrogen are not taken into account [5,36]. Table 1 lists the homogeneous and heterogeneous reactions considered, where the chemical kinetic rate constants are taken from the literature.

The mass conservation equation for the ith biomass particle is written as

$$\frac{dm_i}{dt} = \dot{m}_i = \dot{m}_{vapor,i} + \dot{m}_{devol,i} + \dot{m}_{char,i}, \tag{14}$$

Table 1

Homogeneous and heterogeneous reactions considered in biomass combustion and gasification. Note: $C_{(s)}$ is solid phase char. C_k represents molar concentration of gas species k.

Reference	Homogeneous reactions	Kinetic rate [Kmol/m^3/s]
R1 [31,36]	$CH_4 + H_2O \rightarrow CO + 3H_2$	$R_1 = 0.312 \exp(-15,098/T_g)C_{CH_4}C_{H_2O}$
R2 [31,36]	$CO + H_2O \rightarrow CO_2 + H_2$	$R_2 = 2.5 \times 10^8 \exp(-16,597/T_g)C_{CO}C_{H_2O}$
R3 [31,36]	$CO_2 + H_2 \rightarrow CO + H_2O$	$R_3 = 9.43 \times 10^9 \exp(-20,563/T_g)C_{CO_2}C_{H_2}$
R4 [31,36]	$CH_4 + 2O_2 \rightarrow CO_2 + 2H_2O$	$R_4 = 2.119 \times 10^{11} \exp(-24,379/T_g)C_{CH_4}^{0.2}C_{O_2}^{1.3}$
R5 [31,36]	$CO + 0.5O_2 \rightarrow CO_2$	$R_5 = 1.0 \times 10^{10} \exp(-15,154/T_g)C_{CO}C_{O_2}^{0.5}C_{H_2O}^{0.5}$
R6 [31,36]	$H_2 + 0.5O_2 \rightarrow H_2O$	$R_6 = 2.2 \times 10^9 \exp(-13,109/T_g)C_{H_2}C_{O_2}$
Reference	Heterogeneous reactions	Kinetic rate [s/m]
R7 [40,43]	$C_{(s)} + 0.5O_2 \rightarrow CO$	$R_7 = 0.046 \times 10^7 \exp(-13,523/(R_uT_i))$
R8 [40,43]	$C_{(s)} + H_2O \rightarrow CO + H_2$	$R_8 = 1.71 \times 10^7 exp(-211,000/(R_uT_i))$
R9 [40,43]	$C_{(s)} + CO_2 \rightarrow 2CO$	$R_9 = 9.1 \times 10^6 exp(-166,00/(R_uT_i))$

where $\dot{m}_{vapor,i}$, $\dot{m}_{devol,i}$ and $\dot{m}_{char,i}$ denote the evaporation rate, the devolatilization rate and the char conversion rate, respectively. The moisture evaporation rate is modeled as [31],

$$\dot{m}_{vapor,i} = \frac{ShD_{diff,va}}{d_i}\left(\frac{P_{sat,T_i}}{R_uT_{i,s}} - X_v\frac{p_g}{R_uT_{i,s}}\right)As_iM_v, \tag{15}$$

where Sh is the Sherwood number, which is modeled using Ranz–Marshall correlation, $Sh = (2 + 0.6Re_i^{1/2}Sc^{1/3})$ [44]. Re_i is Reynolds number based on the particle size and relative velocity between the ith particle and the surrounding gas. Sc is the Schmidt number of the surrounding vapor. $D_{diff,va}$, P_{sat,T_i}, As_i, $T_{i,s}$, X_v, and M_v represent respectively the vapor diffusion coefficient, the saturation pressure, the surface area of particle, the surface temperature of the particle, the molar fraction of vapor in the surrounding gas, and the molar weight of vapor. R_u is the universal gas constant. d_i is an equivalent sphere particle diameter computed based on the particle mass m_i and a constant particle density ρ_i, i.e., $d_i = (6m_i/\pi \rho_i)^{1/3}$.

The rate of devolatilization is computed based on the pyrolysis reaction model (Eq. (13)),

$$\dot{m}_{devol,i} = -A_d exp\left(-\frac{E_d}{R_uT_i}\right)m_{volat,i}, \tag{16}$$

where $A_d = 5.0 \times 10^6$ [s^{-1}] and $E_d = 1.2 \times 10^8$ [J/Kmol] are rate constants [5], $m_{volat,i}$ is the mass of the volatile remaining in the particle. These rate constants have been validated under different biomass devolatilization conditions [5,8,21].

The rate of char conversion is computed based on the heterogeneous reactions (R$_7$, R$_8$ and R$_9$) listed in Table 1,

$$\dot{m}_{char,i} = \sum_{j=1}^{3} \dot{m}_{char,ij}, \tag{17}$$

where $\dot{m}_{char,ij}$ represent the char consumption rates by reactions with O_2 ($j = 1$, reaction R7), H_2O ($j = 2$, reaction R8), and CO_2 ($j = 3$, reaction R9),

$$\dot{m}_{char,ij} = -As_ip_j\frac{R_{diff,j}R_{kin,j}}{R_{diff,j} + R_{kin,j}}, \tag{18}$$

$$R_{diff,j} = C_j\frac{[0.5(T_g + T_i)]^{0.75}}{d_i}, \tag{19}$$

$$R_{kin,j} = A_jexp\left(-\frac{E_j}{R_uT_i}\right), \tag{20}$$

where $R_{diff,j}$, $R_{kin,j}$, C_j, T_g, p_j, A_j and E_j represent respectively the diffusion rate coefficient, kinetic rate coefficient, mass diffusion rate constant, gas temperature, partial pressure of the gasifying species in the gas surrounding the particle and Arrhenius rate constants for the char reactions with species O_2, H_2O and CO_2 (cf., R7, R8 and R9 in Table 1). $C_j = 5 \times 10^{-12}$ (s/K$^{0.75}$) [5].

2.2.2. Momentum equations

The kinematics of the ith particle simulated is governed by Newton's second law,

$$d\mathbf{u}_i/dt = \frac{\beta}{\rho_i\theta}(\mathbf{u}_g - \mathbf{u}_i) + \mathbf{g}\left(1 - \frac{\rho_g}{\rho_i}\right) - \frac{1}{\rho_i}\nabla p_g - \frac{1}{\rho_i\theta}\nabla\tau, \tag{21}$$

where $\mathbf{u}_i$, ρ_i, and θ denote respectively the velocity and density of the ith particle, and the solid volume fraction in spatial position $\mathbf{x}_i$ at time t. The right-hand side terms represent the sum of all forces acting on the ith particle by the surrounding gas and particles. The forces considered include, from left to right, the drag, gravity, pressure gradient and the interparticle stress. The virtual mass force, Basset force, and lift force such as the Saffman force and Magnus force, which play a minor role in particle motion, are neglected [29]. With a given $\mathbf{u}_i$, the position of the particle is computed by integration of the equation

$$d\mathbf{x}_i/dt = \mathbf{u}_i. \tag{22}$$

In Eq. (21), the solid volume fraction is modeled as

$$\theta(\mathbf{x}_i, t) = \iint f(m_i, \mathbf{u}_i, \mathbf{x}_i, t)(m_i/\rho_i)dm_id\mathbf{u}_i, \tag{23}$$

where $f(m_i, \mathbf{u}_i, \mathbf{x}_i, t)$ is a particle distribution function, which describes the statistical distribution of mass and velocity of particles in spatial position $\mathbf{x}_i$ at time t. Namely, $f(m_i, \mathbf{u}_i, \mathbf{x}_i, t)dm_id\mathbf{u}_i$ is the average number of particles per unit volume with velocities in the intervals $(\mathbf{u}_i, \mathbf{u}_i + d\mathbf{u}_i)$ and mass in the interval $(m_i, m_i + dm_i)$. In this model, it is assumed that the particle distribution function is independent of particle temperature and composition. This assumption has been widely used in the literature [14,31,45].

In the MP-PIC model f is obtained from the Liouville equation, which is the mathematical expression of conservation of particle numbers per volume moving along dynamic trajectories in the particle phase space [15],

$$\frac{\partial f}{\partial t} + \nabla \cdot (f\mathbf{u}_i) + \nabla_u \cdot (f\mathbf{A}_i) = \frac{f_G - f}{\tau_G} + \frac{f_D - f}{\tau_D}, \tag{24}$$

where $\mathbf{A}_i = d\mathbf{u}_i/dt$ is the acceleration of the particle, f_G is the equilibrium isotropic particle distribution function, f_D is the collision damping particle distribution function, τ_G, τ_D are relaxation times. ∇ and ∇_u are divergence operators with respect to physical space $\mathbf{x}$ and velocity $\mathbf{u}_i$. In Appendix A, further details about these distribution functions, relaxation times and interparticle stress are provided.

The drag force model widely used for the ith individual particle is given by Ku et al. [5], Gidaspow [12], Yang et al. [40]

$$\mathbf{f}_i = \frac{V_i\beta}{\theta}(\mathbf{u}_g - \mathbf{u}_i), \tag{25}$$

where V_i is the volume of the ith particle. In Eqs. (21) and (25), the drag force parameter β is modeled as

$$\beta = \begin{cases} 150\frac{(1-\alpha_g)^2\mu_g}{\alpha_g^2 d_i^2} + 1.75\frac{(1-\alpha_g)\rho_g}{\alpha_g d_i}|\mathbf{u}_g - \mathbf{u}_i| & \alpha_g < 0.8 \\ \frac{3}{4}C_d\frac{(1-\alpha_g)\rho_g}{d_i}|\mathbf{u}_g - \mathbf{u}_i|\alpha_g^{-2.65} & \alpha_g \geq 0.8 \end{cases},$$

(26)

where C_d is the drag coefficient, modeled as [12]

$$C_d = \begin{cases} \frac{24}{Re_i}(1 + 0.15Re_i^{0.687}) & Re_i < 1000 \\ 0.44 & Re_i \geq 1000 \end{cases},$$

(27)

and the particle Reynolds number is defined as

$$Re_i = \alpha_g \rho_g d_i |\mathbf{u}_g - \mathbf{u}_i|/\mu_g.$$

(28)

2.2.3. Energy equation

The particle temperature is obtained from the energy conservation equation for the ith particle,

$$m_i C_{p,i}\frac{dT_i}{dt} = h_i As_i(T_g - T_i) + \frac{\varepsilon_i As_i}{4}(G - 4\sigma T_i^4) \\ -h_{vapor,i}\dot{m}_{vapor,i} - h_{devol,i}\dot{m}_{devol,i} - \sum_{j=1}^{3} h_{i,j}\dot{m}_{char,ij},$$

(29)

where $C_{p,i}$, ε_i, σ, $h_i = (Nu\lambda_{g,s}/d_i)$, and G represent the particle heat capacity, emissivity, Stefan-Boltzmann constant, interphase thermal transfer coefficient, and incident radiation, respectively. $h_{vapor,i}$, $h_{devol,i}$, and $h_{i,j}$ represent the latent heat, the heat of pyrolysis, and heats of char reactions with O_2, H_2O and CO_2, respectively. Nu is the Nusselt number, which is modeled using Ranz–Marshall correlation, $Nu = 2 + 3/5Re_i^{1/2}Pr^{1/3}$ [44,46,47]. Pr is the Prandtl number of the surrounding gas, and $\lambda_{g,s}$ represents thermal conductivity of the surrounding gas. The incident radiation G is obtained from the P-1 radiation model.

2.3. Source terms for particle/gas interaction

In the CGM approach a finite number of virtual particles (hereafter referred as parcels) are simulated. Assume that the number of parcels is N_p. The ith parcel contains multiple real particles; however, all particles have the same properties, i.e., each real particle in the ith parcel has the same mass m_i, velocity $\mathbf{u}_i$, temperature T_i and diameter d_i. The governing equations for the individual real particle in the ith parcel have been presented in Section 2.2.

In the physical space $\mathbf{x}$ at time t, the number of real particles per unit volume that pertain to the ith parcel is n_i. The source terms due to the gas/solid interaction for the continuity equation, momentum equations, enthalpy equation, and the species transport equations are,

$$\bar{S}_m = -\sum_{i=1}^{N_p} n_i\dot{m}_i, \qquad \bar{S}_u = -\sum_{i=1}^{N_p} n_i\mathbf{f}_i \\ \bar{S}_q = -\sum_{i=1}^{N_p} n_i q_i, \qquad \bar{S}_{Y_k} = -\sum_{i=1}^{N_p} n_i\dot{m}_{k,i},$$

(30)

where $\dot{m}_i = \sum_{k=1}^{N} \dot{m}_{k,i}$ is given in Eq. (14), $\mathbf{f}_i$ is given in Eq. (25), $q_i = m_i C_{p,i}\frac{dT_i}{dt}$ is given in Eq. (29), and $\dot{m}_{k,i}$ is due to pyrolysis reaction (Eq. (13)) and char reactions (R7, R8 and R9, Table 1).

2.4. Spatial redistribution of parcels and source terms

In CGM-PCM approach, the solid volume fraction in a given position and time is calculated using Eq. (23) with all particles in the parcels taken into account, and the gas volume fraction is then

$$\alpha_g(\mathbf{x}, t) = 1 - \theta(\mathbf{x}, t).$$

(31)

Physically, $\theta(\mathbf{x}, t) < 1$. However, since a large number of particles are clustered into a single parcel, whose volume could exceed the volume of the local cell, this could lead to $\theta(\mathbf{x}, t) > 1$ or $\alpha_g < 0$, which is non-physical and numerically it can give rise to instability. This issue is particularly true in the most widely used low-cost
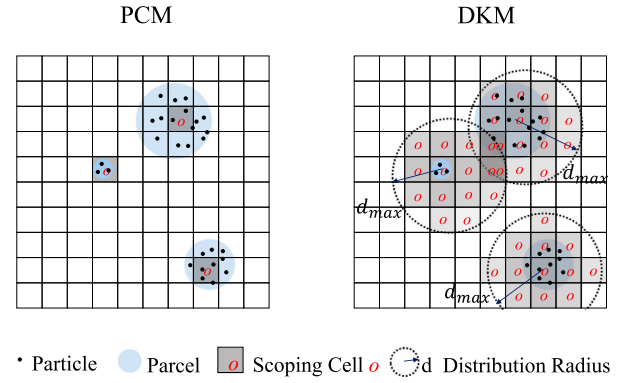

Fig. 1. Schematic illustration of PCM and DKM.

PCM. In the present work, we propose a new method, the so-called distribution kernel method (DKM), which bears similarity to the DBM method, while giving the advantage of the easy implementation and low computational cost. As shown in Fig. 1, the parcels in a PCM computational cell (marked as cell-o) are clusters of sand and biomass particles from the surrounding domain (marked as a circular region). To avoid numerical instability caused by locally too many particles in cell-o, in DKM the particles and the associated source terms in the parcels in cell-o are re-distributed to the surrounding domain from which the particles are clustered. The redistribution algorithm is constructed in such a way that the solid phase volume and source terms in the redistribution domain are conserved before and after distribution.

A filtering kernel function $g(\mathbf{x}, t)$, which is defined based on the distance of the surrounding cells to cell-o, is employed in the present work. The integration of the kernel function over the entire given physical space is unity. Similar strategies were used by Jesse et al. [48], Wang et al. [49], and Sun et al. [22], as well as in our previous work [24]. The surrounding cells of a local cell can be located by a new cell search algorithm based on a given distance, as used in the present work.

The total volume of solid phase in a given domain Ω is given by

$$V_s = \int_{\Omega} \theta_o(\mathbf{x}, t)dV,$$

(32)

where subscript "o" indicates that the quantity is before redistribution. In the following, subscript "r" will be used to denote that the quantity is after redistribution. V_s must stay the same before and after redistribution,

$$V_s = \int_{\Omega} \theta_o(\mathbf{x}, t)dV \equiv \int_{\Omega} \theta_r(\mathbf{x}, t)dV = \int_{\Omega} g(\mathbf{x}, t)V_s dV,$$

(33)

which indicates that the solid volume fraction after redistribution is

$$\theta_r(\mathbf{x}, t) = g(\mathbf{x}, t)V_s = g(\mathbf{x}, t)\int_{\Omega} \theta_o(\mathbf{x}, t)dV,$$

(34)

A simple redistribution function $g'(\mathbf{x}, t)$ is employed,

$$g'(\mathbf{x}, t) = (1 - \frac{|\mathbf{x} - \mathbf{x}_0|}{d_{\max}})^2,$$

(35)

where $\mathbf{x}_0$ is the position of the centroid of cell-o. $d_{\max}$ is a prescribed distance within which solid phase volume and source terms will be redistributed. The function $g'(\mathbf{x}, t)$ may not satisfy Eq. (33). By normalization of $g'(\mathbf{x}, t)$, the filtering kernel function $g(\mathbf{x}, t)$ can be obtained from $g'(\mathbf{x}, t)$,

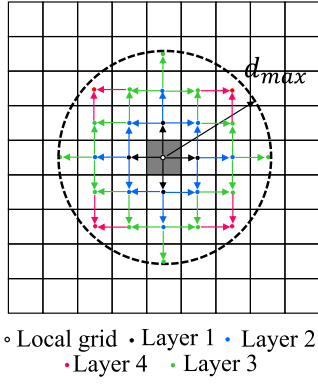$$g(\mathbf{x}, t) = g'(\mathbf{x}, t)/\int_{\Omega} g'(\mathbf{x}, t)dV,$$

(36)

Fig. 2. Cell searching strategy employed in the DKM model.

i.e.,

$$\int_\Omega g(\mathbf{x}, t)dV = 1. \tag{37}$$

$g(\mathbf{x}, t)$ can be used to redistribute the source term for the mass conservation equation,

$$S_{m,r}(\mathbf{x}, t) = g(\mathbf{x}, t)S_M = g(\mathbf{x}, t)\int_\Omega S_{m,o}(\mathbf{x}, t)dV, \tag{38}$$

which is shown to satisfy mass conservation:

$$S_M = \int_\Omega S_{m,o}(\mathbf{x}, t)dV \equiv \int_\Omega S_{m,r}(\mathbf{x}, t)dV = \int_\Omega S_M g(\mathbf{x}, t)dV, \tag{39}$$

Similarly, the source terms for the momentum equations and the energy equation and the species transport equations can be redistributed using $g(\mathbf{x}, t)$:

$$\mathbf{S}_{u,r}(\mathbf{x}, t) = g(\mathbf{x}, t)\int_\Omega \mathbf{S}_{u,o}(\mathbf{x}, t)dV, \tag{40}$$

$$S_{q,r}(\mathbf{x}, t) = g(\mathbf{x}, t)\int_\Omega S_{q,o}(\mathbf{x}, t)dV, \tag{41}$$

$$S_{Y_k,r}(\mathbf{x}, t) = g(\mathbf{x}, t)\int_\Omega S_{Y_k,o}(\mathbf{x}, t)dV. \tag{42}$$

3. Numerical methods and computation cases

The MP-PIC and DKM model are implemented in an open-source CFD code, OpenFOAM v6 [50], based on coalChemistryFoam. The MP-PIC model is adopted in coalCloud for the discrete phase while the solid/gas interaction is taken into account through the source terms in the governing equations of the continuous phase. Structured grid is used in this study. The grid is generated using the "blockMesh" tool provided by OpenFOAM package.

3.1. Implementation of DKM and parallel computation

In the DKM, the surrounding cells within a certain distance to cell-o, d_{max}, are selected for redistribution operations. The cell that is partly located within the sphere of d_{max} is considered to be in the domain of distribution if the distance between the center of the given cell to the center of cell-o is less than or equal to d_{max}. An efficient cell search algorithm is needed, since, the computational cost would increase hugely if all cells are looped during searching. Three search strategies, namely shared-point-based, shared-edge-based and shared-face-based, are used in the present work. As an example, Fig. 2 presents a schematic diagram of the searching procedure of the shared-face-based method. First, the neighboring cells that share one of the faces pertaining to the local cell are selected, cf., the black arrow in Fig. 2. And then, the blue

arrows represent the second layer, and the searching continues until the given maximum distance d_{max}, as shown in Fig. 2, is reached for all the latest selected cells. After each search, the selected cells that are outside of the scope of d_{max} are removed. Note that, in a static mesh and a fixed d_{max}, the search of the neighboring cells is only needed to be performed once.

Since the searching strategy is cell-based without any specific direction, it works perfectly in the unstructured mesh. However, when the simulation domain is decomposed into several sub-domains in a parallel computation, it is not straightforward to search the neighboring cells across sub-domains. Thus, the whole simulation domain is considered in the master processor and the communication between master and slave processors is achieved by applying the message passing interface (MPI).

As an example, as shown in Fig. 3, the domain of redistribution involves four sub-domains in four slave processors. The DKM procedure is done as follows. First, cell searching is performed in the master processor. The solid volume fraction and source terms in cell-o are transferred from the slave processor 2 to the master processor. Then, the source terms of cell-o will be distributed to the cells within the sphere of diameter d_{max} in the master processor. Finally, the distributed source terms are returned to the sub-domains in the slave processors from the master processor.

3.2. Numerical scheme

A finite volume method is used for the numerical solution of the governing equations of the continuous phase. Central difference scheme (CDS) is used for spatial directives and the Crank–Nicolson scheme is used for temporal integration. PIMPLE algorithm, which combines the advantage of PISO (Pressure Implicit with Splitting of Operator) and SIMPLE (Semi-Implicit Method for Pressure-Linked Equations) algorithms, is employed to couple the momentum equations and the continuity equation.

3.3. Case setup, initial and boundary conditions

Two lab-scale fluidized bed reactors are employed to evaluate the MP-PIC model based on the DKM and PCM. The geometries of the two reactors are shown in Fig. 4. The first reactor, hereafter referred to as Case 1, is a bubbling fluidized bed (BFB) reactor where the heat transfer between hot sand particles and cold ambient gas was investigated experimentally [51]. This case is chosen here to evaluate the heat transfer model and the performance of DKM and PCM. The second reactor, hereafter referred to as Case 2, is based on the experiment of biomass combustion and gasification in a lab-scale bubbling fluidized bed furnace [45]. In the original experiment, the furnace has a cylindrical geometry with a 50 mm internal diameter and 1200 mm height. In a previous DEM simulation, the geometry was simplified to a cuboid with an equivalent cross-sectional area [40]. This simplified geometry is chosen here to investigate the biomass combustion model and the performance of DKM and PCM, which enable us to compare directly with the DEM results.

3.3.1. Heat transfer in lab-scale fluidized bed reactor

Particle dynamics and heat transfer in Case 1 are first investigated. As shown in Fig. 4, the BFB reactor has a depth of 15 mm, width of 80 mm and height of 250 mm. The fluidization gas is N_2 with a temperature of 20 °C. The gas is supplied from the bottom of the reactor with three different superficial velocities (U_{sup}). The reactor is initially filled with hot sand particles of 90 °C. The sand particles have a uniform diameter of 1 mm. Table 2 shows the physical properties of the sand particles. Sand temperature (T_s) were measured for five operating conditions with a cold anodized aluminium background wall [51,52]. The total mass of the sand,
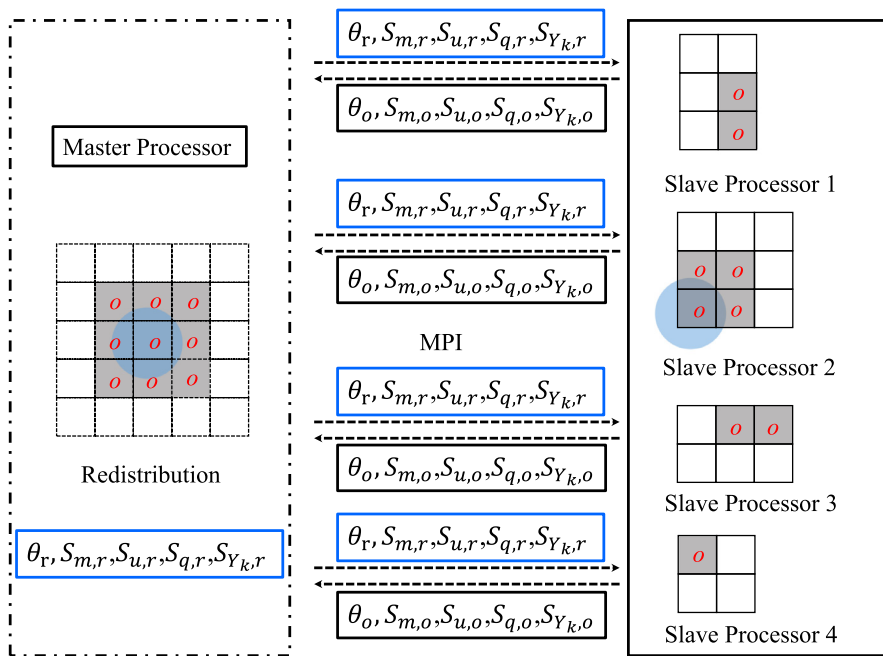
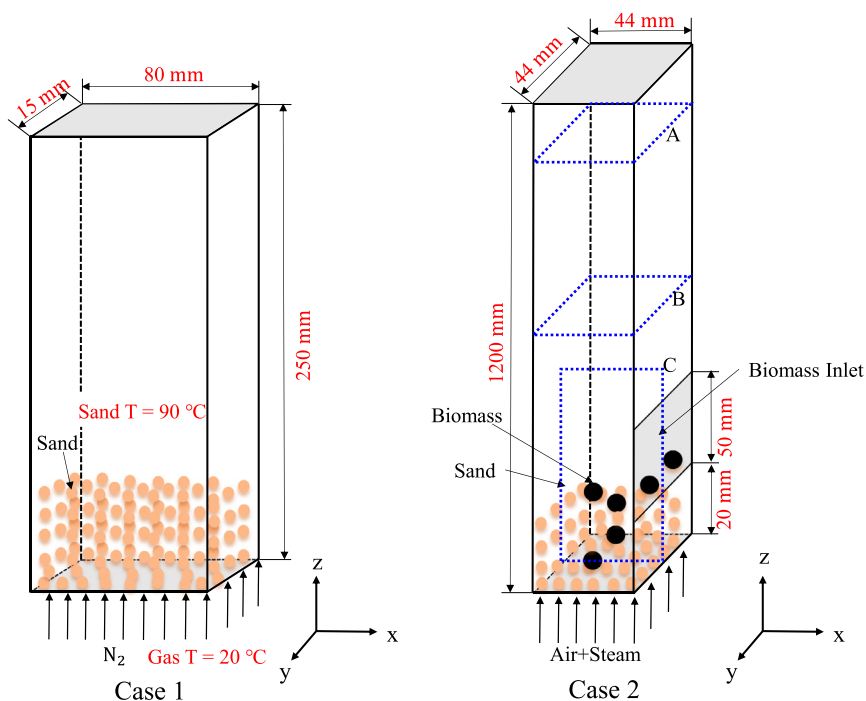**Fig. 3.** Schematic diagram employed in the DKM parallelization.

Fig. 4. Schematic illustration of lab-scale bubbling fluidized bed reactors.

Table 2
Biomass and sand particle properties. *The biomass mass of 0.002 kg is the total mass of biomass injected within 20 s. The biomass is injected to the reactor at a rate of 10^{-4} kg/s.

Cases	Particles	d_i [mm]	ρ_i [kg/m³]	$C_{p,i}$ [J/kg/K]	total mass* [kg]	T_i [°C]
Case 1 [51]	sand	1	2500	840	0.075 & 0.125	90
Case 2 [45]	biomass	$0.25 \sim 0.35$	750	1500	0.002	25
	sand	$0.25 \sim 0.7$	2300	840	1.25	$750 \sim 850$

Table 3

Key parameters and run-cases for the BFB reactor Case 1. The parcel number N_{parcel} is 25024.

Cases	1a	1b	1c	1d	1e	1f	1g	1h
U_{sup} [m/s]	1.33	1.71	1.90	1.33	1.71	1.33	1.33	1.33
m_{sand} [kg]	0.075	0.075	0.075	0.125	0.125	0.100	0.150	0.175
$N_{particle}$ [−]	57,324	57,324	57,324	95,541	95,541	76,433	114,649	133,758
γ [−]	1.32	1.31	1.32	1.56	1.56	1.45	1.66	1.75
$\alpha_{c/p}$ [−]	1.73	1.73	1.73	1.46	1.46	1.57	1.37	1.30

Note: $N_{particle}$ is the real number of particles without CGM.

m_{sand}, was varied from 75 g to 125 g, and the superficial velocity U_{sup}, was varied from 1.33 m/s to 1.90 m/s. Table 3 lists the key parameters of the five experimental cases (Cases 1a – 1e) and three additional cases (Cases 1f-1h) that are simulated to investigate the results with and without DKM.

The outlet boundary is on the top plane of the reactor, cf., Fig. 4. Since the flow close to the outlet is rather uniform, zero gradient of dependent variables has been used as outlet boundary condition (in OpenFoam it is referred to as the 'InletOutlet' boundary condition). The wall boundary is assumed to be non-slip and constant temperature of 20 °C (the same as the gas temperature).

For all cases listed in Table 3, the total number of mesh cells is 23,100 and the number of sand parcels is 25,024. Uniform mesh is used with the cell size of 2.28 mm. The mesh size and parcel number are chosen based on the DEM work of Patil et al. [51]. In the MP-PIC or DEM simulations, the mesh size must be sufficiently larger than the diameter of the particles (without CGM) or the parcels (with CGM). A cell-to-parcel size ratio $\alpha_{c/p}$ is introduced to quantify the size relationship between the mesh and parcels. $\alpha_{c/p}$ is defined as the cube root of the cell volume (V_c) divided by the product of particle/parcel diameter, i.e., $\alpha_{c/p} = \sqrt[3]{V_c}/d_p$, where d_p is the diameter of the particle (without CGM) or the equivalent diameter of the parcel (with CGM). In the CGM, a coarse grain ratio (γ) is defined as the cube root of the number of particles inside a parcel $N_{p/p}$, i.e., $\gamma = \sqrt[3]{N_{p/p}}$.

Numerical instability may arise if $\alpha_{c/p}$ is small [23]. Different values of $\alpha_{c/p}$ have been used in the literature, e.g., 2.5 [11], $1 \sim 4$ [49], 1.58 [53], and stable numerical results were obtained. These values could be difficult to achieve in large scale furnaces with complex geometry since certain small-size cells are needed to discretize the geometry and the quadrillion or more particles are involved in the system, which are clustered to millions of parcels, i.e., in each parcel, there might be millions of sand and biomass particles or more. In Case 1, the ratio of the present cell size to the diameter of parcel $\alpha_{c/p}$ is 1.73, which was selected following the suggestion of a previous work [51]. A value of 1~2 for γ was used in our previous work [21] and 1.44 was employed in Lichtenegger and Miethlinger et al. [53]. For Case 1a – 1e, γ is 1.32 – 1.56, and in each parcel the number of particles is in average about 2~4. For Cases 1g and 1h, higher values of γ are tested to evaluate the performance of DKM at higher solid phase loads.

3.3.2. Combustion and gasification in lab-scale fluidized bed reactor

In Case 2 combustion and gasification of rice husk in a lab-scale bubbling fluidized bed reactor were investigated. As shown in Fig. 4, the biomass inlet has a length of 44 mm and height of 50 mm, and is located at a height of 20 mm above the bottom of the reactor. A mixture of air and steam flows from the bottom of the reactor into the fluidized bed and biomass is injected from the biomass inlet with a feeding rate of 1×10^{-4} kg/s by a screw feeder. Yields of gaseous products at the reactor outlet were measured by Loha et al. [37,45]. Seven cases with different operating conditions were measured (and simulated here) by varying 1) the equivalent air ratio (EAR), which is the ratio of the mass of air to that of dry biomass divided by the stoichiometric ratio of mass of

Table 4

Key parameters studied in Case 2, with different equivalent air ratio (EAR), steam to biomass ratio (SR), and reactor operation temperature (T_r).

Cases	2a	2b	2c	2d	2e	2f	2g
EAR [−]	0.30	0.35	0.40	0.35	0.35	0.35	0.35
SR [−]	0.5	0.5	0.5	0.2	0.8	0.5	0.5
T_r [°C]	800	800	800	800	800	750	850

air to that of dry biomass, 2) the steam ratio SR, which is the ratio of the mass of steam to the mass of dry biomass, and 3) the reactor operation temperature T_r. The furnace is heated by an electric heater and the desired temperature is set through a PID controller [45]. The initial temperature of walls, sand and the gas in the entire domain is the same as the reactor temperature. Air and steam flowing into fluidized bed is preheated to 200 °C, respectively. The EAR was varied from 0.3 to 0.4, the SR was varied from 0.2 to 0.8, and the T_r was varied from 750 °C to 850 °C. Table 4 shows the key parameters of the seven cases. Similar to Case 1, zero gradient boundary condition has been used at the outlet boundary of Case 2 (the top plane of the reactor, Fig. 4). The wall is assumed to be non-slip; the wall has a constant temperature of T_r.

Rectangular uniform mesh is used in the simulation of Case 2. In order to evaluate the sensitivity of the results to the mesh resolution, Case 2b were simulated using three different resolutions, cf. Table 5. The coarse mesh has a cell size of 5.5 mm, and a coarse grain ratio γ of 5.49 for sand parcels and 2.66 for biomass parcels, based on the mean diameters given in Table 2. The medium mesh has a cell size of 4.4 mm, and a coarse grain ratio γ of 4.36 and 2.11 for sand and biomass parcels, respectively. The fine mesh has a cell size of 2.9 mm, and a coarse grain ratio γ of 3.02 and 1.46 for sand and biomass parcels, respectively. The number of parcels were selected in such a way that the cell-to-parcel size ratio $\alpha_{c/p}$ is kept nearly constant for the three meshes, i.e., about 2 for sand parcels and 6.66–6.99 for biomass parcels. As a result, the coarse mesh contains 13,504 cells, with 50,000 sand parcels and 10,000 biomass parcels; the medium mesh contains 26,400 cells, with 100,000 sand parcels and 20,000 biomass parcels; the fine mesh contains 78,300 cells, with 300,000 sand parcels and 60,000 biomass parcels. Other detailed properties of biomass and sand are shown in Tables 2 and 6. The Rosin-Rammler distribution function is employed to model the distribution of particle size. Biomass particle density is assumed to be constant during the conversion process, while the size of the particles decreases during the process. The biomass parcels are injected into the furnace after the sand parcel reaches steady fluidization.

4. Results and discussion

4.1. Heat transfer in lab-scale fluidized bed reactor

The results of Case 1, as described in Table 3, are presented in Fig. 5. This figure shows a comparison for the results of the MP-PIC model with PCM, the results of a previous work [51] with

Table 5

Mesh sensitivity study for Case 2b and key parameters. The coarse grain ratio γ is calculated based on the mean diameter of particles in the parcel. N_{parcel} for biomass is the total number of parcel injected within 20 s.

Cases	Cell size [mm]	N_{parcel} (sand & biomass)	$\alpha_{c/p}$ (sand & biomass)	γ (sand & biomass)
Coarse mesh	5.5	50,000 & 10,000	2.00 & 6.89	5.49 & 2.66
Medium mesh	4.4	100,000 & 20,000	2.01 & 6.94	4.36 & 2.11
Fine mesh	2.9	300,000 & 60,000	1.92 & 6.60	3.02 & 1.46

Table 6

Biomass properties in Case 2 [45].

Ultimate analysis	[wt.%]	C	H	O	N	S	Ash
		38.43	2.97	36.36	0.07	0.49	21.68
Proximate analysis	[wt.%]	Volatile	Fixed Carbon	Moisture	Ash		
		55.54	14.99	9.95	19.52		
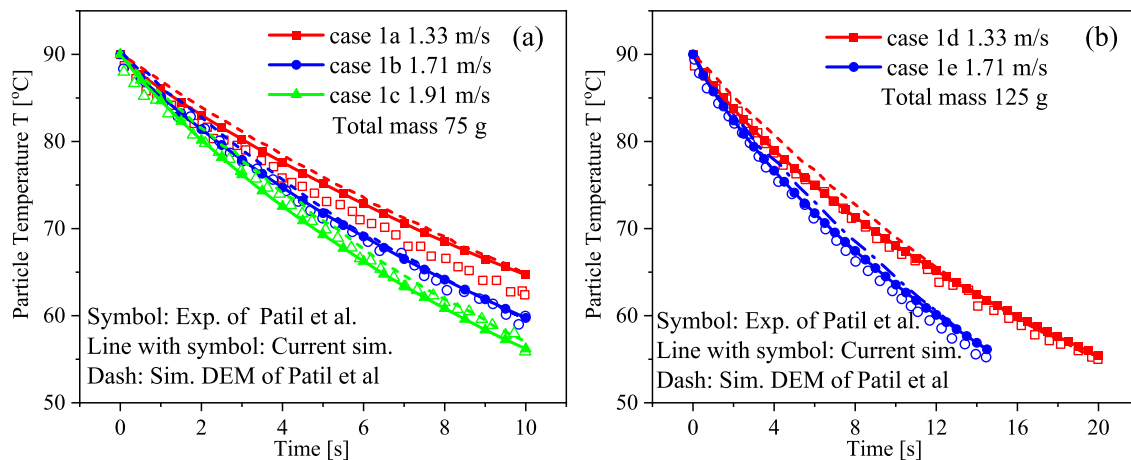
Fig. 5. Comparison of mean particle temperature between the present simulations using the PCM (solid lines), and previous simulations using the DEM approach (dashed lines) [51], as well as with experiments (circles) [52] for the five cases (Cases 1a – 1e) with the total sand mass of 75 g (a) and 125 g (b) and various superficial N_2 velocity.

a more expensive DEM approach, and the experimental measurements [52] for the five cases 1a–1e. As shown in Fig. 5, the present PCM results agree very well with the DEM results and the experiments. The maximum error of the results of the current model (in comparison with experiments) at $t = 10$ s is less than 5%, which occurs for Case 1a ($U_{sup} = 1.33$ m/s, $m_{sand} = 75$ g). The convective and radiative heat transfer between the solid particles and the ambient gas, radiative heat transfer between particles, and the conductive heat transfer between particles and walls are taken into account in the heat transfer mechanisms of the model (Eq. (29)). The mean particle temperature decreases faster as the superficial velocity U_{sup} increases and the slope dT_i/dt decreases over time. Higher U_{sup} leads to higher gas phase mass flux and enhanced mixing of sand and the cold N_2 gas, and as a result, a faster decrease of the mean particle temperature. The last three terms on the right-hand side of Eq. (29) are zero, since the sand particles are chemically inert. The temperature difference $T_g - T_i$ decreases with time, which results in a decreasing slope of particle temperature since the convective heat transfer plays a leading role. dT_i/dt is approximately proportional to $T_g - T_i$, Eq. (29). Due to the low operation temperature in Case 1 ($\leq 90^oC$), the radiative heat transfer plays an insignificant role. The particle temperature predicted with radiative heat transfer is nearly identical to that without radiative heat transfer.

The temperature distributions for gas and particles for two different U_{sup} with the m_{sand} of 75 g are shown in Fig. 6. At the start of the process, $t = 2$ s, high temperature gradient near the bottom of the reactor and near the walls results in a high temperature on the top of the bed. At a later time, $t = 8$ s, the sand particles tend to gather near the wall because the gas-solid interactions and

particle-particle collision drive the parcels to flow toward the wall, and then descend along the wall. The high temperature particles near the wall increased the gas temperature near the wall.

As mentioned in Section 2.4, DKM is proposed to handle the situation when the fluidized bed is under over-loading conditions. In order to demonstrate the performance of DKM under over-loading conditions, the results from the MP-PIC model with PCM and DKM are compared. Figure 7 shows the transient development of the mean particle temperature in Case 1 with the superficial velocity $U_{sup} = 1.33$ m/s and mass of sand particles ranging from 75 g to 175 g. The simulations are based on the number of parcels and meshes of Case 1 as listed in Table 3 (Cases 1a, 1d, 1f–1h). As the mass of sand increases from 75 g to 175 g, the carrier load $1/\alpha_{c/p}$ varies from 0.58 to 0.77. When the mass of sand is increased to 175 g (Case 1h), PCM suffers from numerical instability and no results could be obtained. It is shown that PCM can predict the transient heat transfer process up to $m_{sand} \leq 150$ g. DKM can very well predict the transient heat transfer process at this high load condition. Figure 7 shows that for the cases where both PCM and DKM are applicable, the results from the two methods agree with each other very well.

4.2. Combustion and gasification in lab-scale fluidized bed reactor

The results from the numerical simulations using MP-PIC model for the lab scale bubbling fluidized bed, Case 2 in Table 4, are presented here. Initially, the reactor is filled with sand particles up to $z = 0.1$ m; after reaching steady operation the bubbling fluidized bed has a height of about 0.22 m [37]. The biomass combustion/gasification process occurs mainly in the lower 0.5 m of
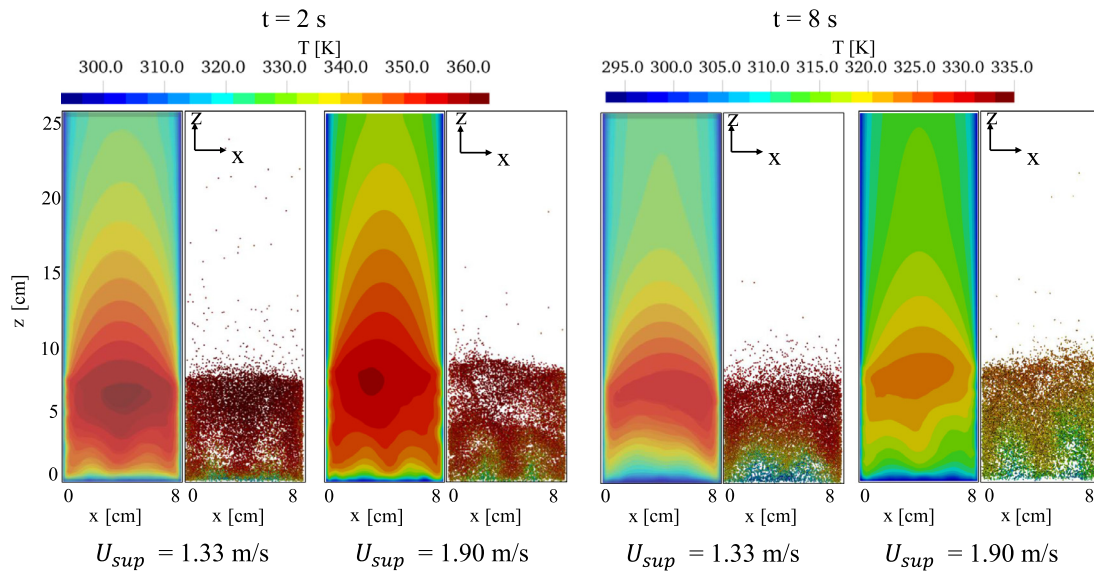
Fig. 6. Gas temperature, sand particle temperature, and distribution of sand parcels with PCM at 2s and 8s of Case 1a and Case 1c.
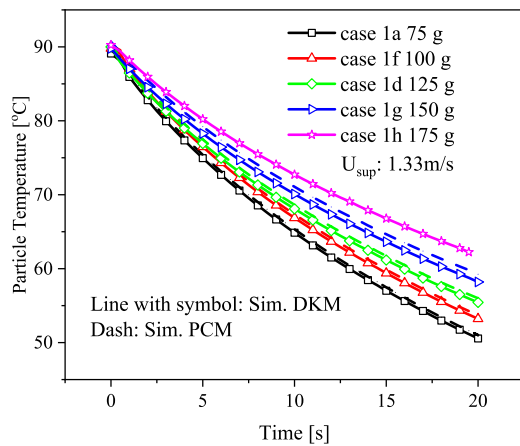

Fig. 7. Temporal evolution of particle temperature in Case 1. Comparison between PCM and DKM with different carrier loads.

the reactor. Figure 8 shows the temporal evolution of mean mass fractions of N_2, CO_2, CO, H_2, and CH_4 averaged over cross section planes at two different heights of the reactor ($z = 0.6$ m and $z = 1.1$ m) for Case 2b, simulated using PCM with three different mesh resolutions (Fig. 8a and b), and the PCM and DKM approaches with the medium mesh (Fig. 8c and d). The two sampling cross sections are indicated in Fig. 4 as plane A and plane B. In the initial transient stage the biomass particles undergo heating, pyrolysis, partial oxidation and gasification, during which the mass fractions of gaseous products (CO_2, CO, H_2, and CH_4) increase while the mass fraction of inert gas N_2 decreases. After a short time, the reactor reaches steady operation. For the data sampled at the of plane $z = 0.6$ m, steady results are reached at 5 s, whereas at the $z = 1.1$ m plane steady results are reached after 7 s. It is clear that the results from the three meshes agree very well; the results from PCM and DKM agree also well during both the transient stage and the steady operation stage. The difference between the PCM and DKM results increases with time in the transient stage, i.e., the difference increases as the thermochemical conversion process progresses. When the process is in the steady stage, the difference between the PCM and DKM results does not change significantly with time. As will be discussed later, the PCM model suffers from certain loss of the biomass mass in the local over-loading cells. This results in a lower mass fraction of species that are generated from the biomass, i.e., CH_4, CO, H_2 and CO_2, and a higher mass fraction of N_2. The difference between the results from the different meshes is smaller than that from PCM and DKM. Based on the convergence behavior of the results with three different meshes, the medium mesh was employed in the simulations of cases 2a–2g.

Figure 9 shows the distribution of sand particles and sand temperature in the 3D domain of the lower 200 mm region of the reactor. The biomass inlet is located on the right side of the domain, $20 \text{ mm} \leq z \leq 70 \text{ mm}$. Due to the heat exchange with cold biomass particles, the temperature of sand particles is lower in the region where biomass particles are mixed with sand particles. Initially, the biomass particles flow together with sand particles upward near the right side wall (0.9–1 s). When the biomass parcels are injected into the reactor, a small gas bubble can be found around the biomass inlet. The biomass particles are squeezed into the near-wall zone by the sand particles due to lower momentum of the biomass particles than the sand particles. The particles with low density and small size tend to move toward the edge of the bubble and the upper part of the bed because of the particle-particle collision and the gas-solid interactions.

At $t = 1$s, the biomass particles start to spread into the center of the reactor due to the particle/particle collision. As the biomass particles move near the wall, the drag force become smaller due to the lower carrier velocity $\mathbf{u}_g$. In addition to the drag force, the motion of the particles is driven by the gravity $\mathbf{g}$ and pressure gradient ∇p (Eq. (21)). The particles descend along the wall until collision force from other particles and higher pressure from the bottom of the bed becomes dominant. Then, the particles can escape the near-wall zone and move to the full fluidization region. From $t = 1.1$ s to 1.5 s, the biomass particles appear to interact with the sand particles and the surrounding gas only in the bottom 200 mm region of the reactor. Certain gas bubbles (regions without any particles) can be found at $t = 1.4$ s–1.5 s (in the upper right corner of the domain in Fig. 9).

Figure 10 shows the distribution of gas temperature and mass fractions of key species at $t = 20$ s in a cross section plane near the biomass inlet. The shown cross section is in the middle plane of the reactor, in a region from the bottom of the reactor to a height of 200 mm. The region is marked as C in Fig. 4, where the biomass inlet on the right side of the domain is also indicated. The gas tem-
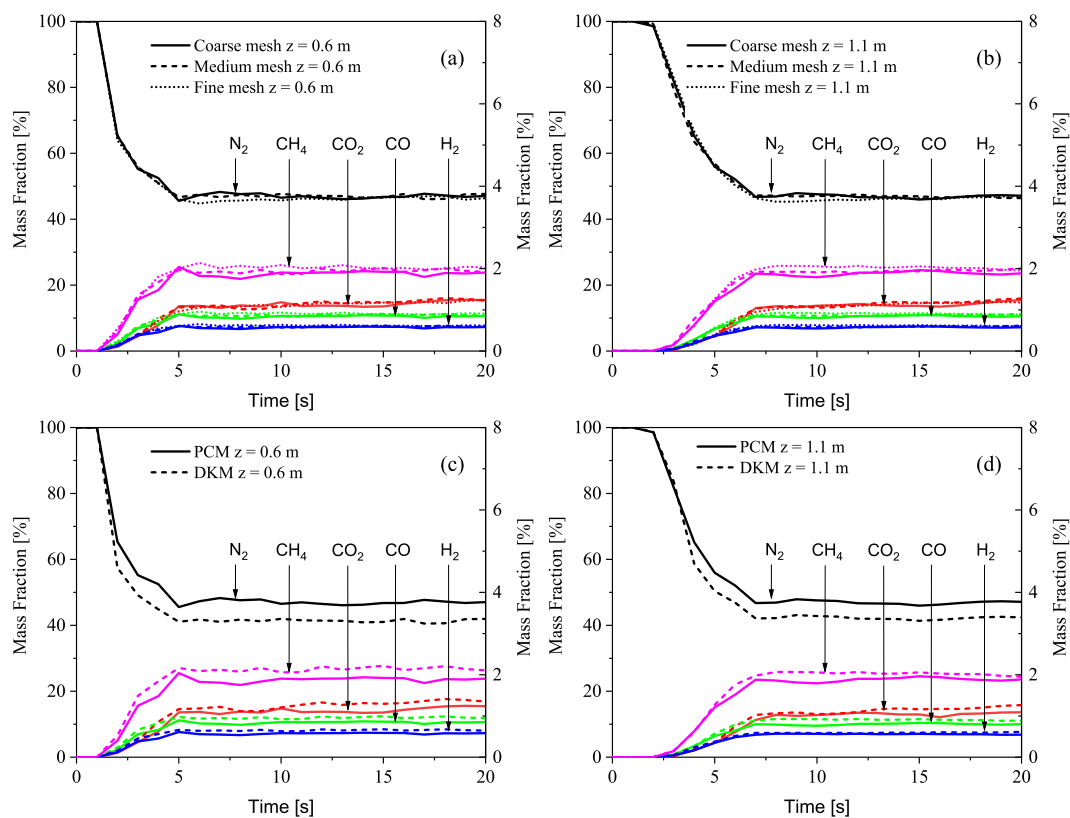
Fig. 8. Temporal evolution of gas product mass fractions over time with different meshes and number of parcels taken from the cross sections at the height of (a, c) 0.6 m and (b, d) 1.1 m for Case 2b. Values of N_2, CO_2, and CO mass fractions are shown on the left vertical axis while H_2 and CH_4 on the right vertical axis. The results are from the MP-PIC model with PCM and three different meshes (a, b) and from the MP-PIC model with PCM and DKM using the medium mesh (c,d).
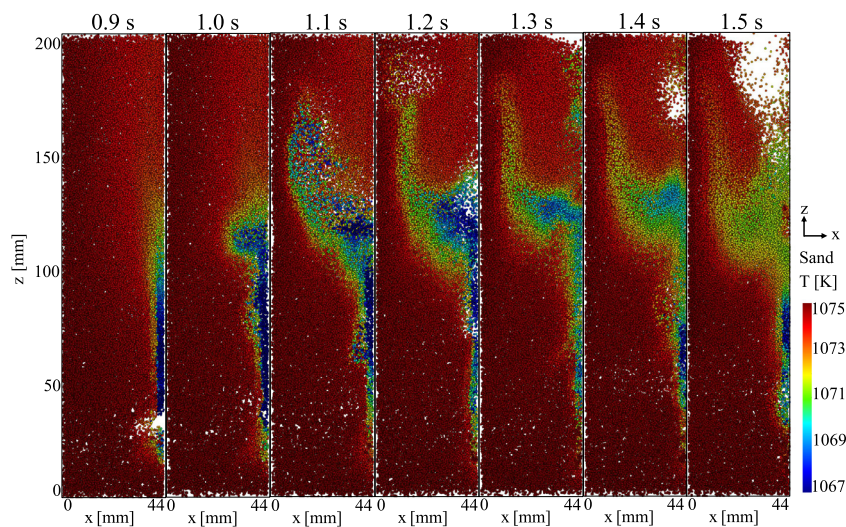

Fig. 9. Distribution of sand particles and sand temperature of Case 2b during the initial development stage of the reactor, simulated using MP-PIC with PCM.

perature is rather uniform, with slightly low temperature in the region near the biomass inlet, which corresponds to the cooling by the cold biomass particles. Oxygen is shown to be consumed quickly in the lower region of the bed, by reacting with volatile gases CO, CH_4 and H_2, forming CO_2. Higher mass fractions of CO, CH_4 and H_2 can be seen in the right side of the reactor, above the biomass inlet, indicating the region where the pyrolysis and gasification reactions take place.

In the present bubbling fluidized bed reactor, the mass of the biomass particles is only 0.16% of the total mass of solid phase within the 20 s period of operation (cf., Table 2). Thus, com-

pared with the convective and radiative heat transfer, the heat release/loss due to combustion, pyrolysis and gasification is relatively insignificant in affecting the particle temperature and the gas temperature. This is the reason that the particle temperature and gas temperature are fairly homogeneous in space and nearly the same as that of the reactor operation temperature, cf., Figs. 9 and 10.

Figure 11 shows a comparison of steady-state product gas mole fractions at the reactor outlet obtained from the simulations and experiments for the seven cases listed in Table 4. The effect of equivalent air ratio (EAR) on the product gas is shown in Fig. 11a and d. When EAR is increased from 0.3 to 0.4, the yields of H_2,
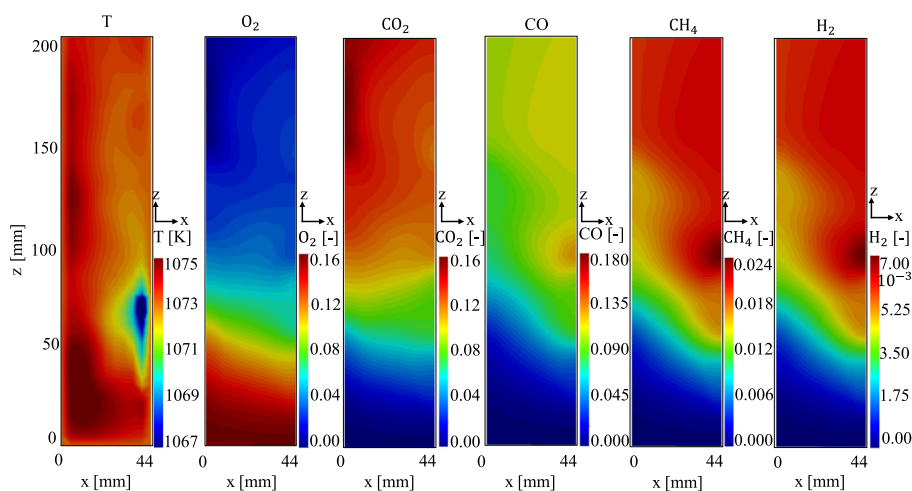
Fig. 10. Distribution of gas temperature, and mass fractions of O_2, CO_2, CO, H_2 and CH_4 in Case 2b at 20 s, simulated using MP-PIC with PCM.
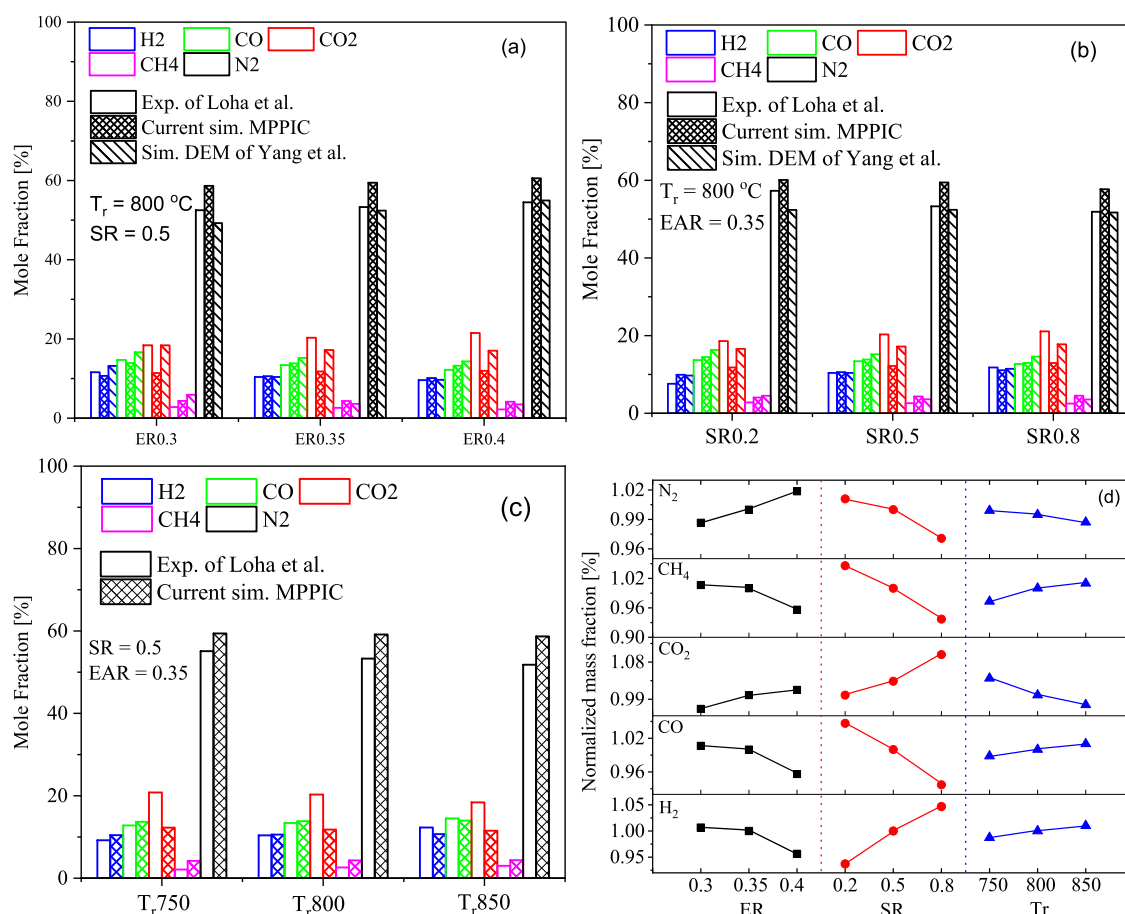

Fig. 11. Comparison of the mole fractions of product gas between the MP-PIC/PCM simulations (pattern fill), the previous simulations using the DEM approach [40] (slash fill), as well as with experiments (blank fill) [45] for seven cases (Cases 2a - 2g) at different operation conditions: (a) SR 0.5, T_r 800 °C with various EAR: 0.30, 0.35, 0.40, (b) EAR 0.35, T_r 800 °C with various SR: 0.2, 0.5, 0.8, and (c) EAR 0.35, SR 0.50 with various T_r: 750 °C, 800 °C, 850 °C. In (d), the results from the MP-PIC/PCM simulations are re-plotted to show the trend of the product gas, where the gas mass fractions have been normalized by the corresponding results of Case 2b.

CH_4, and CO decrease and the yields of the CO_2 and N_2 increase. This trend is shown in the experimental data and confirmed with the model predictions, although the effect of EAR on the predicted results is relatively weaker. This trend can be explained using the combustion/gasification reaction model shown in Table 1, where it is shown that an increasing supply of air to the reactor (increasing EAR) will enhance the oxidation of H_2, CH_4, and CO, which results in an increasing CO_2 yield.

As shown in Fig. 11b and d, when SR increases, the yields of CH_4, CO and N_2 decrease and the yields of H_2 and CO_2 increase. This is because the higher amount of steam in the reactor promotes the water-gas shift reaction (reaction R2), the gasification reaction with H_2O (reaction R8), and the methane/water reaction (reaction R1), cf., Table 1. It is observed that higher operation temperature T_r results in higher yields of H_2, CH_4, and CO, and lower yields of the CO_2 and N_2, Fig. 11c and d. This can be at-
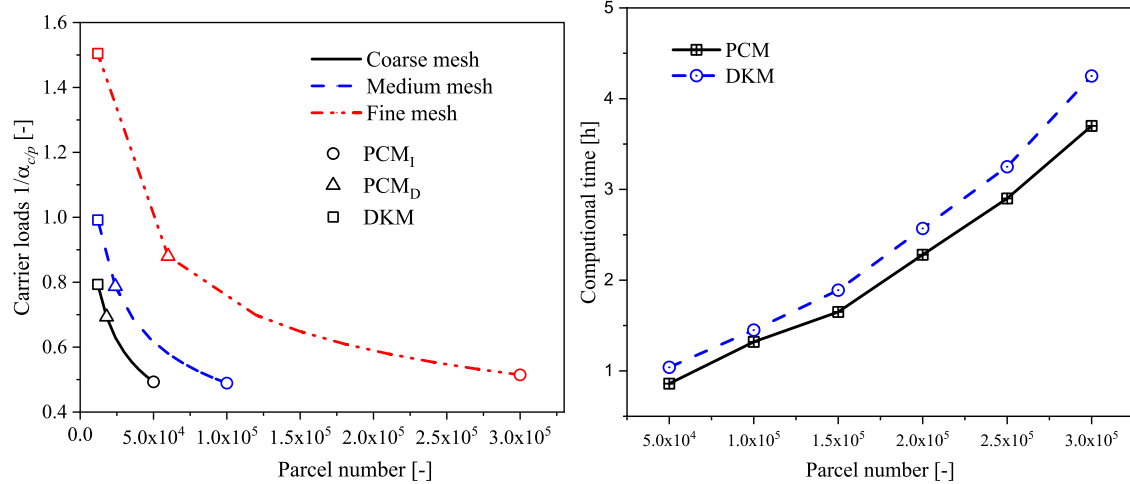
Fig. 12. Carrier loads under which stable solution exists for Case 2b. Subscript "I" indicates the baseline setup given in Table 4; subscript "D" indicates the condition close to numerical instability. Lines with symbol in the right figure indicate the computational time required to simulate the combustion/gasification process for 1 s of physical time.

tributed to the enhanced gasification/oxidation reactions of char, Table 1.

Apart from the comparison with the experimental measurements, the MP-PIC model results are compared with the DEM results of Yang et al. [40]. It is shown that, the computational time required in the MP-PIC simulations is significantly shorter than that in the DEM simulations. With a similar number of mesh cells and processors (64 processors), the DEM simulation required 73 days to simulate a physical time of 20 s of the combustion/gasification process [40], whereas the present MP-PIC simulations required less than 2 days (with a Xeon E5-2698v3 Haswell 2.3 GHz CPU). Despite the significantly lower computational cost of MP-PIC model compared with the DEM, the results from MP-PIC model agree very well with the experiments and the DEM results for most species, except for CO_2 and N_2. Comparing with the experimental results, the average relative error for H_2 and CO predicted from MP-PIC is 9.13% and 5.94%, respectively. The relative error of CH_4 is high, which can be attributed to the simplified pyrolysis model and the absence of tar in the model [5], and the low concentration of CH_4 in the product gas.

The results from PCM and DKM, and the numerical stability and computational cost of DKM and PCM are evaluated under the EAR, SR and T_r condition of Case 2b. The number of parcels and mesh resolution are varied. When the number of sand parcels is changed, the number of biomass parcels is modified accordingly (the number of biomass parcels is 20% of that of the sand parcels). As shown in Fig. 12, the carrier load increases as the number of parcels decreases. For a given number of parcels, the fine mesh has a higher carrier load. Each symbol denotes a simulation case that is numerically stable and in which converged solution is obtained. For PCM, the simulation case with maximum carrier load that a stable numerical solution is obtained is marked with triangles. The maximum carrier load for the coarse, medium and fine meshes is 0.69, 0.79 and 0.88, respectively. For DKM, stable numerical solution can be obtained at much higher carrier loads. The medium mesh can have a carrier load close to 1, and the fine mesh can allow for overloading parcels, e.g., with a carrier load of 1.5.

Physically, a carrier load close to 1 means that the cell is filled with solid particles, and a carrier load larger than 1 is not possible. However, numerically, this situation is unavoidable due to irregular small-size CFD cells in complex fluidized bed boiler geometries. In DKM, the contribution of local over-loading to the solid volume fraction and source terms are redistributed to the surrounding cells (Eqs. (38)–(42)). Thus, the DKM offers a more

robust method that allows for achieving numerical solution with local carrier over-loading. With the cell searching strategy shown in Figs. 2 and 3, the DKM is computationally efficient. The cases with different numbers of sand parcels are tested in parallel computation with 128-core to obtain results for a physical time of 1 s and the running time of each case is shown in Fig. 12. The computational efficiency tends to decline as the number of parcels in the computational domain increases. The increase in computational time of DKM is within 20% of that for PCM.

Since the source term is redistributed in the DKM, the results from DKM and PCM could be different. Figure 7 shows that, for Case 1, the difference between PCM and DKM results is noticeable but not significant. Figure 13 shows the predicted product gas mole fractions for Case 2 with PCM and DKM based on the medium mesh. The results with 50,000 sand parcels (and 10,000 biomass parcels) are labeled as PCM_L and DKM_L; and the results with 100,000 sand parcels (and 20,000 biomass parcels) are marked as PCM and DKM. As shown in Fig. 13, the DKM results are less sensitive to the number of parcels than the PCM results. The maximum relative error between PCM and PCM_L is 12.6%, while the DKM and DKM_L is less than 5.5%. The DKM results agree also better with the experiments than the PCM results, in particular for CO_2 and N_2.

The gas phase governing equations are invalid when the gas volume fraction is negative. The maximum load of solid in a CFD cell is thus limited. The theoretical maximum solid volume fraction of a sphere of diameter d_p in the cube of side length of d_p is $\pi/6 \sim 0.52$. Considering the impact of the collision deformation, and the filling of the void by extremely small size particles, the maximum solid volume fraction is about 0.62 [22,37]. This is the maximum pack limit of particles in a cell. If the solid volume fraction exceeds the maximum pack limit, either the results become non-physical or numerical instability may occur. In PCM, it is often that solid volume fraction is set to the maximum pack limit, if it is above the limit. This will result in a loss of solid mass. The finer the mesh, the worse the situation can become [24]. As shown in Fig. 13, the loss of biomass in the over-loading cells gives rise to the under-prediction of CO_2 mass fraction from PCM as compared with the experiments, and the over-prediction of mass fraction of N_2. The DKM results are in better agreement, due to source term redistribution that mitigates the loss of biomass in the over-loading cells. For the same reason, the loss of biomass is likely the reason of the lower gas product mole fractions of H_2, CO, and CH_4 predicted by PCM, cf., Fig. 11.
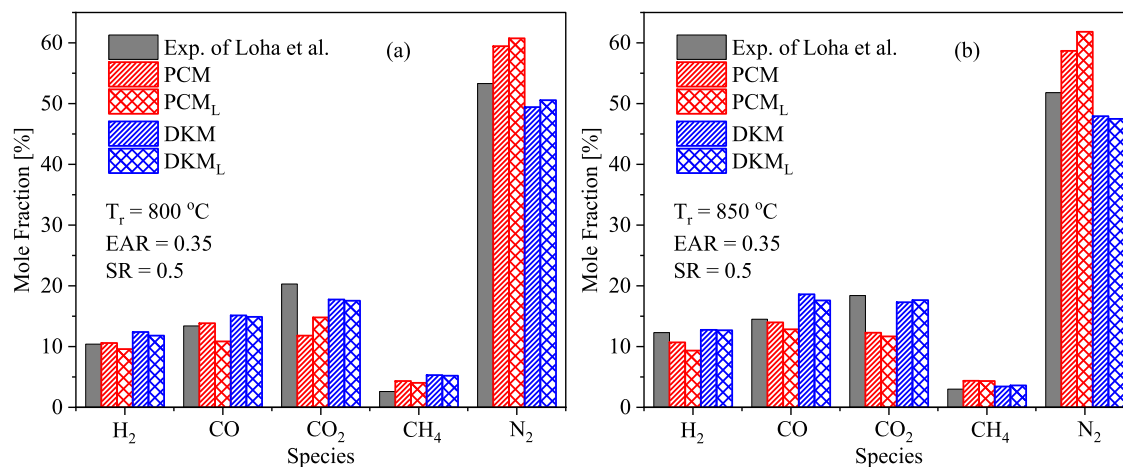
Fig. 13. Mole fractions of product gases from experiments and numerical simulations using PCM and DKM for Case 2b with different parcel numbers.

The loss of solid mass in the PCM simulation due to local over-loading is indirectly related to the "loss" of the solid volume fraction (θ), which is a result of the numerical implementation of the maximum pack limit. The mass of the solid phase that is solved in the discrete phase Eq. (14) is not affected by the loss of θ, since the maximum pack limit is applied to θ but not directly to the solid mass (m_i). For the same reason, the source terms (Eq. (30)) of the gas phase governing equations are not affected explicitly. Instead, the source terms are reduced implicitly due to the change of gas volume fraction (α_g). From Eqs. (1) to (4) it appears that an increase of α_g is equivalent to a decrease of the source terms from solid biomass conversion. Since α_g increases when θ is decreased, the mass of gas produced from biomass conversion is decreased.

To confirm the above discussion, the total mass of sand particles in the reactor of Case 2 is evaluated in two different ways. First, the total mass of sand (M_s) is computed from the discrete phase,

$$M_s = \sum_{i=1}^{N_s} m_{s,i}$$

where N_s is the total number of sand parcels and $m_{s,i}$ is the mass of the ith sand parcel. It is found that M_s is 1.25 kg, i.e., conserved in the process. Second, M_s is computed from the solid volume fraction

$$M_s = \rho_s \int_\Omega \theta(\mathbf{x}, t) dV$$

where ρ_s is the density of sand particles and Ω is the entire domain of the reactor. Since the mass of biomass is only 0.16% of the total mass of the solid phase within the 20 s period of operation (cf., Table 2), it is expected that M_s computed from the second method should be only slightly higher than that from the first method, with an increase less than 0.0016(ρ_s/ρ_b), i.e., 0.49% (where ρ_b is the density of biomass particles). It is found that M_s from the PCM simulations of Case 2b (shown in Fig. 13) computed using the second method fluctuates in time around a mean value of 1.12 kg, which is about 10.4% reduction of the sand mass. DKM can significantly mitigate the loss of θ. For Case 2b the DKM results show a loss of M_s by a mean value of 4%. The loss of θ in DKM is also due to the numerical implementation of the maximum pack limit. In the future study, the DKM redistribution scheme needs to be further improved to avoid the local over-loading to exceed the maximum pack limit.

5. Conclusion

In the present work, a three-dimensional MP-PIC model was developed for numerical simulation of heat transfer and biomass combustion/gasification process in fluidized bed reactors. The conventional MP-PIC method is based on the particle centriod method (PCM) and coarse grain method (CGM), which is computationally efficient but suffers from local over-loading if the CFD cell is fine or if locally small-size cells are used. The latter is typically encountered in studies of fluidized bed furnaces with complex geometries. A distribution kernel method (DKM) is proposed to replace PCM, aiming to improve the accuracy and robustness of the method. The following conclusions are drawn:

- The DKM approach can effectively handle the over-loading problem of PCM. It is shown that the PCM simulation becomes unstable if the carrier load is high, while DKM can allow for significantly higher carrier load without suffering from numerical instability. This enables the use of local small-size cell typically encountered in simulation of fluidized bed boilers with complex geometries.
- For low carrier load conditions, e.g., Case 1 studied in this work, the DKM and PCM results agree with each other very well. At high carrier load conditions, e.g., Case 2 studied in this work, the DKM approach gives an improved prediction of the product gas yields from biomass combustion/gasification, in comparison with the PCM approach. It is found that the DKM results are less sensitive to the number of parcels than the PCM approach.
- The present MP-PIC/DKM approach can capture the transient heat transfer process and biomass combustion/gasification process of bubbling fluidized bed reactors. The DKM can be further improved by allowing for dynamic selection of the distance of redistribution kernel.

Declaration of Competing Interest

The authors declare that they have no known competing financial interests or personal relationships that could have appeared to influence the work reported in this paper.

Appendix A. Solid phase collision model

The interparticle stress in Eq. (21) is difficult to resolve for each particle in dense flows [14]. The model of Lun et al. [54] is employed to model the contact normal stress τ in Eq. (21),

$$\tau = [\theta \overline{\rho}_i + \theta^2 \overline{\rho}_i (1+e)g_0] \frac{1}{3} \langle C^2 \rangle \tag{A.1}$$

$$g_0 = \frac{3}{5}[1 - (\frac{\theta}{\theta_{sp}})^{\frac{1}{3}}]^{-1} \tag{A.2}$$

where g_0, $\overline{\rho}_i$, e and θ_{sp} represent respectively the radial distribution function, the mean density of particles in a local cell, the coefficient of restitution, the close pack volume fraction, and C represents the instantaneous minus the hydrodynamic velocity of the particle [14].

The first term in the RHS of Eq. (24) models the collision return-to-isotropy effect and the second term models the collision damping effect. Physically, particle collision tends to damp out the velocity fluctuations and it is assumed that within a damping relaxation time τ_D the particle velocity will approach to a mean value,

$$\overline{\mathbf{u}}_i = \int f m_i \mathbf{u}_i dm_i d\mathbf{u}_i / \int f m_i dm_i d\mathbf{u}_i, \tag{A.3}$$

and the distribution function $f(m_i, \mathbf{u}_i, \mathbf{x}_i, t)$ will approach to $f_D(m_i, \mathbf{u}_i, \mathbf{x}_i, t)$. The collision damping particle distribution function $f_D(m_i, \mathbf{u}_i, \mathbf{x}_i, t)$ is given by O'Rourke and Snider [18], 19]

$$f_D(m_i, \mathbf{u}_i, \mathbf{x}_i, t) = \delta(\mathbf{u}_i - \overline{\mathbf{u}}_i) \int f d\mathbf{u}_i, \tag{A.4}$$

where δ is a Dirac function.

A competing process is that the particle collision could result in a Gaussian distribution of particle velocity occurring within a relaxation time τ_G, which is described by the equilibrium isotropic particle distribution function $f_G(m_i, \mathbf{u}_i, \mathbf{x}_i, t)$,

$$f_G(m_i, \mathbf{u}_i, \mathbf{x}_i, t) = G(\mathbf{u}_i; \overline{\mathbf{u}}_i, \sigma^2) \int f d\mathbf{u}_i, \tag{A.5}$$

where G is a Gaussian velocity distribution with the mean $\overline{\mathbf{u}}_i$ and variance σ^2. σ^2 can be obtained by enforcing that the variance of f_G is equal to that of f.

The relaxation time τ_D in the damping collision model is modeled as O'Rourke and Snider [18],

$$\frac{1}{\tau_D} = \frac{8\sqrt{2}}{3\pi} \frac{\theta}{r_{32}^3} \frac{\sum_i N_i (r_i + r_{32})^4 (\mathbf{u}_i - \overline{\mathbf{u}}_i)^2}{\sum_i N_i (r_i + r_{32})^2 \sqrt{(\mathbf{u}_i - \overline{\mathbf{u}}_i)^2}} g_0(\theta) \eta (1 - \eta). \tag{A.6}$$

The relaxation time τ_G in the isotropic collision model is [19],

$$\frac{1}{\tau_G} = \frac{8\sqrt{2}}{5\pi} \frac{\theta}{r_{32}^3} \frac{\sum_i N_i (r_i + r_{32})^4 (\mathbf{u}_i - \overline{\mathbf{u}}_i)^2}{\sum_i N_i (r_i + r_{32})^2 \sqrt{(\mathbf{u}_i - \overline{\mathbf{u}}_i)^2}} g_0(\theta) \eta (2 - \eta). \tag{A.7}$$

where r_{32} and r_i is Sauter mean radius and effective particle radius, respectively. $g_0(\theta)$ is a factor given by $\theta_{sp}/(\theta_{sp} - \theta)$. η is defined as $(1 + e)/2$.

References

[1] M. Van de Velden, J. Baeyens, I. Boukis, Modeling CFB biomass pyrolysis reactors, Biomass Bioenergy 32 (2) (2008) 128–139.

[2] A.V. Bridgwater, Renewable fuels and chemicals by thermal processing of biomass, Chem. Eng. J. 91 (2–3) (2003) 87–102.

[3] H. Fatehi, W. Weng, Z. Li, X.-S. Bai, M. Aldén, Recent development in numerical simulations and experimental studies of biomass thermochemical conversion, Energy Fuels 35 (9) (2021) 6940–6963.

[4] K. Luo, F. Wu, S. Yang, M. Fang, J. Fan, High-fidelity simulation of the 3-D full-loop gas–solid flow characteristics in the circulating fluidized bed, Chem. Eng. Sci. 123 (2015) 22–38.

[5] X. Ku, T. Li, T. Løvås, CFD-DEM simulation of biomass gasification with steam in a fluidized bed reactor, Chem. Eng. Sci. 122 (2015) 270–283.

[6] W. Yang, D. Pudasainee, R. Gupta, W. Li, B. Wang, L. Sun, An overview of inorganic particulate matter emission from coal/biomass/MSW combustion: sampling and measurement, formation, distribution, inorganic composition and influencing factors, Fuel Process. Technol. 213 (2021) 106657.

[7] S. Ozgen, S. Cernuschi, S. Caserini, An overview of nitrogen oxides emissions from biomass combustion for domestic heat production, Renew. Sustain. Energy Rev. 135 (2021) 110113.

[8] S. Wang, K. Luo, C. Hu, J. Fan, CFD-DEM study of the effect of cyclone arrangements on the gas-solid flow dynamics in the full-loop circulating fluidized bed, Chem. Eng. Sci. 172 (2017) 199–215.

[9] J. Wang, Continuum theory for dense gas-solid flow: astate-of-the-art review, Chem. Eng. Sci. 215 (2020) 115428.

[10] T.B. Anderson, R. Jackson, Fluid mechanical description of fluidized beds. equations of motion, Ind. Eng. Chem. Fund. 6 (4) (1967) 527–539.

[11] Y. Tsuji, T. Kawaguchi, T. Tanaka, Discrete particle simulation of two-dimensional fluidized bed, Powder Technol. 77 (1) (1993) 79–87.

[12] D. Gidaspow, Multiphase Flow and Fluidization: Continuum and Kinetic Theory Descriptions, Academic Press, 1994.

[13] M. Lungu, J. Siame, L. Mukosha, Comparison of CFD-DEM and TFM approaches for the simulation of the small scale challenge problem 1, Powder Technol 378 (2021) 85–103.

[14] D.M. Snider, An incompressible three-dimensional multiphase particle-in-cell model for dense particle flows, J. Comput. Phys. 170 (2) (2001) 523–549.

[15] M.J. Andrews, P.J. O'Rourke, The multiphase particle-in-cell (MP-PIC) method for dense particulate flows, Int. J. Multiph. Flow 22 (2) (1996) 379–402.

[16] P.J. O'Rourke, P.P. Zhao, D. Snider, A model for collisional exchange in gas/liquid/solid fluidized beds, Chem. Eng. Sci. 64 (8) (2009) 1784–1797.

[17] C.H. Kruger, W.G. Vincenti, Introduction to Physical Gas Dynamics, John Wlley & Sons, 1965.

[18] P.J. O'Rourke, D.M. Snider, et al., An improved collision damping time for MP-PIC calculations of dense particle flows with applications to polydisperse sedimenting beds and colliding particle jets, Chem. Eng. Sci. 65 (22) (2010) 6014–6028.

[19] P.J. O'Rourke, D.M. Snider, Inclusion of collisional return-to-isotropy in the MP-PIC method, Chem. Eng. Sci. 80 (2012) 39–54.

[20] J.E. Hilton, P.W. Cleary, Comparison of non-cohesive resolved and coarse grain DEM models for gas flow through particle beds, Appl. Math. Model. 38 (17–18) (2014) 4197–4214.

[21] T. Qi, T. Lei, B. Yan, G. Chen, Z. Li, H. Fatehi, Z. Wang, X.-S. Bai, Biomass steam gasification in bubbling fluidized bed for higher-H_2 syngas: CFD simulation with coarse grain model, Int. J. Hydrog. Energy 44 (13) (2019) 6448–6460.

[22] R. Sun, H. Xiao, Diffusion-based coarse graining in hybrid continuum–discrete solvers: theoretical formulation and a priori tests, Int. J. Multiph. Flow 77 (2015) 142–157.

[23] Z. Peng, E. Doroodchi, C. Luo, B. Moghtaderi, Influence of void fraction calculation on fidelity of CFD-DEM simulation of gas-solid bubbling fluidized beds, AIChE J. 60 (6) (2014) 2000–2018.

[24] J. Zhang, T. Li, H. Ström, T. Løvås, Grid-independent Eulerian–Lagrangian approaches for simulations of solid fuel particle combustion, Chem. Eng. J. 387 (2020) 123964.

[25] M. Farzaneh, S. Sasic, A.-E. Almstedt, F. Johnsson, D. Pallarès, A novel multigrid technique for Lagrangian modeling of fuel mixing in fluidized beds, Chem. Eng. Sci. 66 (22) (2011) 5628–5637.

[26] P. Jenny, D. Roekaerts, N. Beishuizen, Modeling of turbulent dilute spray combustion, Prog. Energy Combust. Sci. 38 (6) (2012) 846–887.

[27] H. Watanabe, A. Matsuo, A. Chinnayya, K. Matsuoka, A. Kawasaki, J. Kasahara, Numerical analysis of the mean structure of gaseous detonation with dilute water spray, J. Fluid Mech. 887 (2020) A4, doi:10.1017/jfm.2019.1018.

[28] D.A. Lysenko, I.S. Ertesvåg, K.E. Rian, Numerical simulation of non-premixed turbulent combustion using the eddy dissipation concept and comparing with the steady laminar flamelet model, Flow Turbul. Combust. 93 (4) (2014) 577–605.

[29] Z.Y. Zhou, S.B. Kuang, K.W. Chu, A.B. Yu, Discrete particle simulation of particle-fluid flow: model formulations and their applicability, J. Fluid Mech. 661 (2010) 482–510, doi:10.1017/S002211201000306X.

[30] J. Chomiak, A. Karlsson, Flame liftoff in diesel sprays, Symp. (Int.) Combust. 26 (1996) 2557–2564. Elsevier

[31] L. Yan, C.J. Lim, G. Yue, B. He, J.R. Grace, Simulation of biomass-steam gasification in fluidized bed reactors: model setup, comparisons and preliminary predictions, Bioresour. Technol. 221 (2016) 625–635.

[32] D. Neves, H. Thunman, A. Matos, L. Tarelho, A. Gómez-Barea, Characterization and prediction of biomass pyrolysis products, Prog. Energy Combust. Sci. 37 (5) (2011) 611–630.

[33] C. Di Blasi, Combustion and gasification rates of lignocellulosic chars, Prog. Energy Combust. Sci. 35 (2) (2009) 121–140.

[34] P.E.A. Debiagi, G. Gentile, M. Pelucchi, A. Frassoldati, A. Cuoci, T. Faravelli, E. Ranzi, Detailed kinetic mechanism of gas-phase reactions of volatiles released from biomass pyrolysis, Biomass Bioenergy 93 (2016) 60–71.

[35] H. Fatehi, W. Weng, M. Costa, Z. Li, M. Rabaéal, M. Aldén, X.-S. Bai, Numerical simulation of ignition mode and ignition delay time of pulverized biomass particles, Combust. Flame 206 (2019) 400–410.

[36] L. Yan, Y. Cao, H. Zhou, B. He, Investigation on biomass steam gasification in a dual fluidized bed reactor with the granular kinetic theory, Bioresour. Technol. 269 (2018) 384–392.

[37] C. Loha, H. Chattopadhyay, P.K. Chatterjee, Three dimensional kinetic modeling of fluidized bed biomass gasification, Chem. Eng. Sci. 109 (2014) 53–64.

[38] R.I. Singh, A. Brink, M. Hupa, CFD modeling to study fluidized bed combustion and gasification, Appl. Therm. Eng. 52 (2) (2013) 585–614.

[39] J.C. Wurzenberger, S. Wallner, H. Raupenstrauch, J.G. Khinast, Thermal conversion of biomass: comprehensive reactor and particle modeling, AIChE J. 48 (10) (2002) 2398–2411.

[40] S. Yang, H. Wang, Y. Wei, J. Hu, J.W. Chew, Numerical investigation of bubble dynamics during biomass gasification in a bubbling fluidized bed, ACS Sustain. Chem. Eng. 7 (14) (2019) 12288–12303.

[41] H. Fatehi, M. Costa, X.-S. Bai, Numerical study on K/S/Cl release during devolatilization of pulverized biomass at high temperature, Proc. Combust. Inst. 38 (3) (2021) 3909–3917.

[42] H. Fatehi, Z.S. Li, X.S. Bai, M. Aldén, Modeling of alkali metal release during biomass pyrolysis, Proc. Combust. Inst. 36 (2) (2017) 2243–2251.

[43] M.B. Nikoo, N. Mahinpey, Simulation of biomass gasification in fluidized bed reactor using ASPEN PLUS, Biomass Bioenergy 32 (12) (2008) 1245–1254.

[44] W.E. Ranz, W.R. Marshall, Evaporation from drops, part I, Chem. Eng. Prog. 48 (1952) 141−146.

[45] C. Loha, H. Chattopadhyay, P.K. Chatterjee, Energy generation from fluidized bed gasification of rice husk, J. Renew. Sustain. Energy 5 (4) (2013) 043111.

[46] W.E. Ranz, W.R. Marshall, Evaporation from drops, part II, Chem. Eng. Prog. 48 (1952) 173−180.

[47] A. Vepsäläinen, S. Shah, J. Ritvanen, T. Hyppänen, Bed sherwood number in fluidised bed combustion by Eulerian CFD modelling, Chem. Eng. Sci. 93 (2013) 206–213.

[48] J. Capecelatro, O. Desjardins, An Euler–Lagrange strategy for simulating particle-laden flows, J. Comput. Phys. 238 (2013) 1–31.

[49] Z. Wang, Y. Teng, M. Liu, A semi-resolved CFD-DEM approach for particulate flows with kernel based approximation and hilbert curve based searching strategy, J. Comput. Phys. 384 (2019) 151–169.

[50] Openfoam foundation, Openfoam-the open source CFD tool box-user guide (version 6), (https://cfd.direct/openfoam/user-guide/).

[51] A.V. Patil, E. Peters, J. Kuipers, Comparison of CFD-DEM heat transfer simulations with infrared/visual measurements, Chem. Eng. J. 277 (2015) 388–401.

[52] A.V. Patil, E. Peters, V.S. Sutkar, N.G. Deen, J. Kuipers, A study of heat transfer in fluidized beds using an integrated DIA/PIV/IR technique, Chem. Eng. J. 259 (2015) 90–106.

[53] T. Lichtenegger, T. Miethlinger, On the connection between Lagrangian and Eulerian metrics for recurrent particulate flows, Phys. Fluids 32 (11) (2020) 113308.

[54] C.K.K. Lun, S.B. Savage, D.J. Jeffrey, N. Chepurniy, Kinetic theories for granular flow: inelastic particles in Couette flow and slightly inelastic particles in a general flowfield, J. Fluid Mech. 140 (1984) 223−256, doi:10.1017/S0022112084000586.